CZECH TECHNICAL UNIVERSITY IN PRAGUE
Faculty of Electrical Engineering
Department of Electromagnetic Field

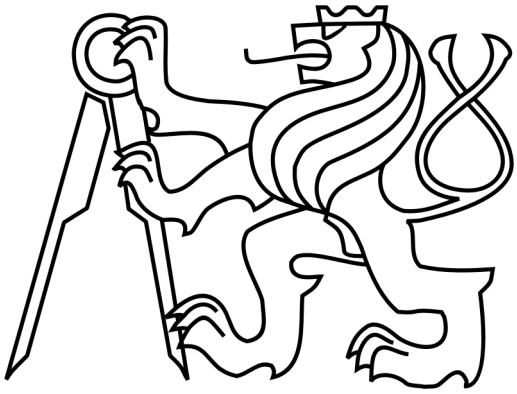

Determination of Spatial Density Profile of Tungsten in Magnetically Confined Hot Plasmas

Student: Matěj Tomeš M.Sc.
Supervisor: Prof. Miloš Mazánek
Assoc. Prof. Jan Mlynář

Master Thesis
May 2014

Zadání

Místo této stránky vložit zadání práce

Abstract

Soft x-ray tomography is a non-invasive method of obtaining information about various properties of hot plasma. Tomographic algorithms can deliver values of radiation intensity in the whole plasma cross-section. This is convenient in case of fusion reactors using magnetic confinement where the plasma temperature forbids any way of direct measurements, e.g. by Langmuir probes. A hot plasma tomography is being used at JET. The current system consist of two pinhole cameras measuring soft x-ray radiation in horizontal and vertical directions. Due to construction restrictions of JET, the cameras are placed in different toroidal sections and the thickness of the beryllium wall between the camera and the plasma differs. The thickness of the beryllium separating cameras from the plasma is $250\mu m$ and $350\mu m$ for the camera with vertical and the camera with horizontal orientation, respectively. Beryllium acts as a filter for radiation within the soft x-ray band. The different thicknesses cause the spectral sensitivities of cameras to vary. This introduces unwanted errors in tomographic reconstruction. This is due to the fact that the the overall intensity measured by both cameras is different. This effect is amplified by the presence of impurities in the plasma. Parts of JET inner wall which are to be in the most contact with the plasma are made of tungsten. Due to its high atomic number, tungsten is not stripped of all electrons even in the hottest parts of the plasma and the line radiation of tungsten in the recorded soft x-ray band is significant. The line radiation amplifies the differences in intensities recorded by soft x-ray cameras which also has a negative effect on tomographic reconstructions. It is known that errors in reconstructions are dependent on plasma temperature and presence of impurities. These two properties are not constant in the plasma cross section. The goal of this thesis is to suggest a way of calculating correction coefficients compensating for the errors caused by different spectral sensitivities of soft x-ray cameras and to estimate density profiles of tungsten. Spectra generated by hot plasma in the frequency band of interest are modelled for both cases of pure plasma and plasma containing tungsten impurities. Analytically derived formulas and atomic data provided by OPEN-ADAS are used. Based on the spectral models estimates of tungsten densities can be made. An Algorithm delivering values of correction coefficients is developed. Values of corrections coefficients are estimated for four tomographic reconstructions and the dependence on electron temperature and tungsten

density is studied.

Abstrakt

Tomografie měkkého rentgenového záření je neinvazivní metodou, která umožňuje získávat hodnoty intenzity záření v průřezu plazmatu. Této vlastnosti se využívá v případě měření na tokamacích, kde teplota plazmatu znemožňuje využívání některých metod měření, jako například pomocí Langmuirových sond. Tomografie měkkého rentgenového záření se využívá i na tokamaku JET. Tomografický systém na JET se skládá ze dvou kamer měřících měkké rentgenové záření v horizontálním a vertikálním směru. Z důvodů konstrukčního řešení vakuové komory reaktoru jsou tloušťky beryliové zdi oddělující kamery od plazmatu odlišné. Tloušťka berylia je v případě vertikální kamery 250μm a v případě horizontální kamery 350μm. Berylium se v pásmu měkkého rentgenového záření chová jako filtr. Rozdílné tloušťky zdi reaktoru oddělující kamery tak zapříčiňuje rozdílné spektrální citlivosti obou kamer, které tak neposkytují totožné naměřené intenzity záření. To zapříčiňuje chyby v tomografických rekonstrukcích řezu plazmatu. Části vnitřní zdi reaktoru, pro které se předpokládá častý kontakt s plazmatem, jsou konstruovány z wolframu. Wolfram je těžký kov s vysokou teplotou tání. Atomy wolframu nejsou plně ionizovány ani při nejvyšších teplotách dosahovaných ve středu reaktoru. Pokud se tedy v plazmatu nacházejí tyto nečistoty, jejich čárové záření je značné. To může ještě zesílit chyby v tomografických rekonstrukcích způsobené rozdílnou spektrální citlivostí kamer. Je známo, že velikost chyb je závislá na teplotě plazmatu a na hustotách iontů wolframu. Cílem této práce je navrhnout výpočet korekcí pro tomografické rekonstrukce, snižující chyby způsobené rozdílnou spektrální citlivostí kamer, a určení prostorového rozložení hustoty wolframu. Modely spektrálních charakteristik měkkých rentgenových záření vytvářených v plazmatu jsou vytvořeny pomocí analitycky odvozených vztahů a pomocí atomových dat dostupných v databázi OPEN-ADAS. Tyto modely jsou dále využity pro stanovení vlivu spektrálních citlivostí kamer na měřené intenzity, což umožňuje určit prostorové rozložení hustoty wolframu a navrhnout hodnoty korekcí pro tomografické rekonstrukce.

Prohlášení

Prohlašuji, že jsem předloženou práci vypracoval samostatně a že jsem uvedl veškeré použité zdroje v souladu s Metodickým pokynem o dodržováni etických principů při přípravě vysokoškolských závěrečných prací.

Datum:12.5. 2014 Matěj Tomeš

Acknowledgements

As first I would like to thank to Prof. Miloš Mazánek for taking me under his wings and for being my supervisor at the Czech Technical University in Prague.

My gratitude goes to Assoc. Prof. Jan Mlynář who gave me the opportunity to work on this interesting topic. I would like to thank him for his patient supervision, support and all those fruitful consultations.

I send my deepest thanks to my dear friend Mathias Scheele who went through the hell of proofreading huge parts of this thesis work and who tried to cheer me up during my ups and downs. If he ever dares to open this report again:"Mate, I owe you one!!!"

I would also like to thank my beloved sister Karolina for her support during the last days of writing this thesis. My gratitude goes also to the rest of my family, without your endless support I would have never made it so far.

Contents

List of Figures

List of Tables

Nomenclature

ℓ	orbital quantum number
$\hbar$	reduced Planck constant $\hbar = 1.05 \cdot 10^{-34} J \cdot s$
K_0	modified Bessel function of the second kind
r	position vector
ν	frequency
ω	angular frequency
Ψ	wave function
$\varepsilon_{i \to j}$	Emission in a spectral line $\varepsilon_{i \to j}$
ζ	ion charge
A	ion state
e	electron charge $e = 1.6 \cdot 10^{-19} C$
E_x	energy
h	Planck constannt $h = 6.63 \cdot 10^{-34} J \cdot s$
k	Boltzman constant $k = 1.38 \cdot 10^{-23} J K^{-1}$
m	index referring a combination of quantum numbers m_ℓ, ℓ
m_ℓ	magnetic quantum number
m_e	electron mass $m_e = 9.10 \cdot 10^{-31} kg$
m_s	spin quantum number
$P(\zeta, m)$	Population probability of ion state ζ, m

$PEC^{(exc)}$ Photon Emissivity Coefficient via electron impact excitation

R_y Rydberg constant $Ry = 13.6\,eV$

R_{fb} Radiation coefficient of free-bound radiation $[Wcm^3]$

R_{ff} Radiation coefficient of free-free radiation $[Wcm^3]$

S Radiation power density $[Wcm^{-3}]$

R Radiation coefficient. Power radiated per electron per ion per unit volume $[Wcm^3]$.

Chapter 1

Introduction to Nuclear Fusion, Magnetic Confinement & Tomography of Hot Plasma

1.1 Nuclear Energy

Energy released in a nuclear reaction comes from an increase of a binding energy difference of initial and final nuclei [1]. An atom nucleus consists of Z protons and N neutrons. The energy binding the nucleus can be obtained comparing sum of masses of protons m_p and neutrons m_n in the nucleus and the nuclear mass m_a of the nucleus as a whole. It shows that

$$Nm_n + Zm_p > m_a \tag{1.1}$$

the nuclear mass is smaller than the sum of masses of individual nucleons. This difference in mass can be explained by the binding energy, an energy needed to split the nucleus. The value of the binding energy can be obtained from the mass difference using Einstein's formula, which relates mass and energy

$$E_B = (Nm_n + Zm_p - m_a)\, c^2 \tag{1.2}$$

Using the latter equation and values for masses from tab. 1.1, the value of binding energy for α particle is $E_B = 28.29MeV$. Binding energies of all other elements can be obtained the same way. In fig. 1.1 a curve showing calculated values of binding energies per nucleon vs. atomic mass of elements is shown [1]. There is a number of conclusions to be drawn from its shape. The binding energy of elements is the highest for the group of elements with intermediate mass number and drops for elements with both higher and lower mass number. Elements with mass number close to iron $A \approx 56$ are not suitable to be used in nuclear energy for two reasons. The energy release in a nuclear reaction corresponds to the difference in the binding energies of the initial

Element	Symbol	Mass number A	Charge number Z
Electron	e	0.000549	-1
Neutron	n	1.008665	0
Hydrogen (Proton)	$_1H^1$,p	1.007276	1
Deuterium	$_1H^2$,D	2.013353	1
Tritium	$_1H^3$,T	3.015501	1
Helium-3	$_2He^3$	3.014933	2
Helium-4 (alpha)	$_2He^4$,α	4.001503	2

Table 1.1: Properties of nuclei of light elements involved in fusion reaction. Mass is given in units of atomic mass, charge in electron charge.Reprinted from [1].

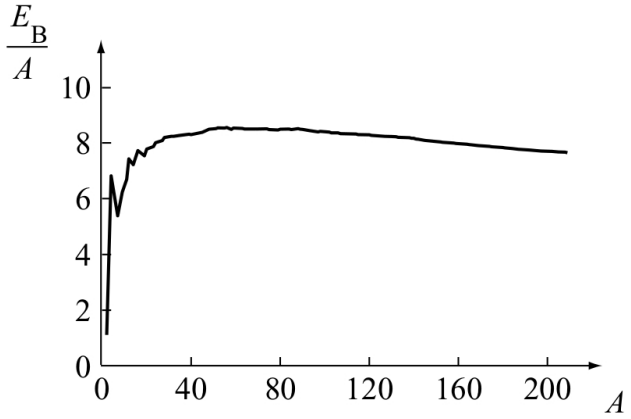

Figure 1.1: Binding energies in MeV per nucleon vs. mass number for the dominant form of each chemical element.Reprinted from [1]

and final elements [2]. The derivative of binding energy curve with respect to the mass number is the lowest for $A \approx 56$ and thus the energy realeased during reactions is low. The second reason is the initiation of the reactions is difficult, due to the high binding energy. For these reasons, nuclear reactions of light or heavy elements are more suitable to be used as energy sources. The initiation of the reaction is easier due to the lower binding energy and the energy outcome in the reaction is higher. In eq. (1.3) examples of nuclear fusion of light elements D and T and fusion reaction including Chromium are given together with energies released.

$$\begin{aligned} D + T &\rightarrow {}_2He^4 + n + 17.6MeV \\ {}_8O^{16} + {}_8O^{16} &\rightarrow {}_{14}Si^{28} + \alpha + 1.9MeV \end{aligned} \tag{1.3}$$

The dependence of the shape of the binding energy curve in fig. 1.1 is given by an equilibrium between two forces acting upon particles in the atomic nucleus. The first

is weak long-range Coulomb force and the second is strong short-range nuclear force. The increase in binding energy with the increase of mass number of light elements is connected to the growing nuclear force [1]. The saturation of the binding energy is caused by the short-range nature of the nuclear force. With increasing number of protons in an atomic nucleus, both nuclear force and dimensions of the nucleus grow. When the nucleus reaches a certain size, the nuclear force between two most distant protons becomes negligible. The further increase of number of protons in the nucleus makes the Coulomb force dominate over the nuclear force and the binding energy of the nucleus decreases. A derivation of approximative formulas for values of nuclear and Coulomb forces in nucleus as a function of mass number is given in [1].

1.1.1 Thermonuclear Fusion

In order to fuse two atomic, they have to be brought into a distance over which the attractive nuclear force overcomes the repulsive Coulomb force. This distance is in orders of the size of an atomic nuclei. The dependence of the potential energy of two colliding nuclei as a function of their distance is shown in fig. 1.2. In the classical

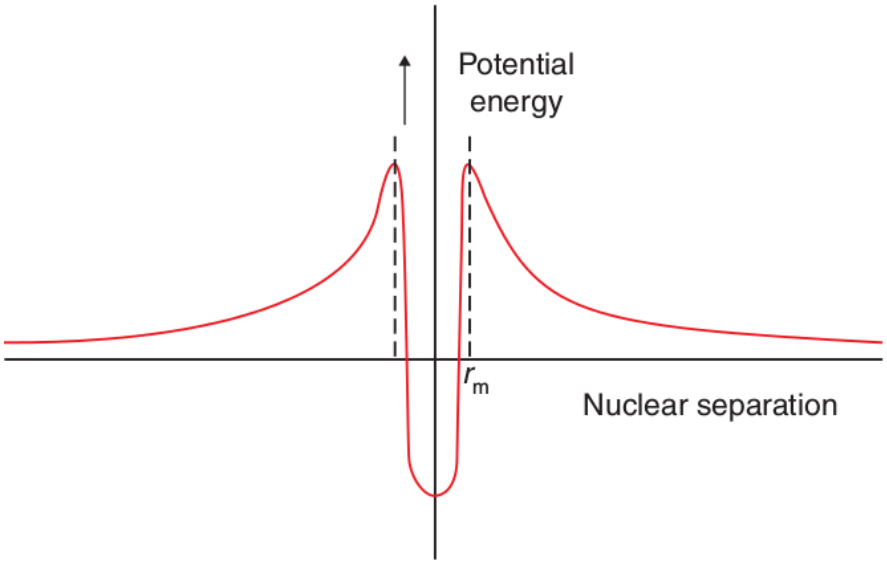

Figure 1.2: A diagram showing dependence of potential energy of two colliding atomic nuclei. The repulsive Coulomb force increases as the nuclei come closer to each other up to a distance r_m, where the potential energy has its maximum. At this distance the attractive nuclear force takes over and the potential energy drops. Reprinted from [2].

picture two nuclei would not fuse together if the initial kinetic energy of the particles

before collision is lower than the maximum of potential energy given by:

$$E_{min} = \frac{q^2}{4\pi\varepsilon_0 r_m} \tag{1.4}$$

Fusion can occur for particles with initial kinetic energy somewhat lower than the potential energy given by $eq : Pot_e n$. This is due to the quantum mechanical tunneling effect. The probability of two particles undergoing a fusion can be characterized by a quantity called cross-section, the meaning is described for example in [1]. Cross-section is a function of energy of colliding particles. It has units of area and is specific for each combination of colliding species. The cross-section is not a monotonous function of energy. The position of maximum value of cross-section depends on the species of colliding particles. In fig. 1.3 experimentally obtained cross-sections for three kinds of fusion reactions are plotted. A good way of comparing the convenience of different

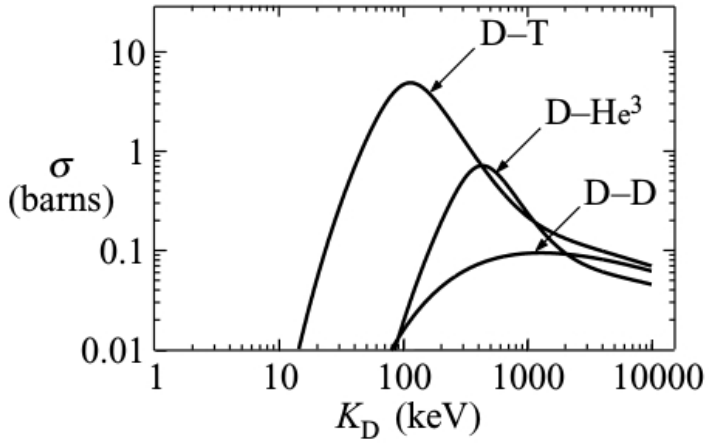

Figure 1.3: Experimentally obtained cross-sections for three kinds of fusion reactions: deuterium-tritium $(D-T)$, deuterium-helium $(D-{}_2He^3)$ and deuterium-deuterium $(D-D)$. Cross-sections are plotted as functions of deuteron energy $K_D = 1/2 m_D v_D^2$. Reprinted from [1].

fusion reactions is comparing the fusion reaction rate R and the power density S. The reaction rate gives number of fusion reactions occurring in a unit volume per unit time. Multiplied by the energy E_f released in a single fusion event, the reaction rate can be used to calculate power density. Averaging over velocity distribution of both species the fusion reaction rate and power density is[1]:

$$S = E_f R_{12} = E_f n_2 n_1 \iint \sigma(|\mathbf{v}_1 - \mathbf{v}_2|)|\mathbf{v}_1 - \mathbf{v}_2| f(\mathbf{v}_1) f(\mathbf{v}_2) \mathrm{d}\mathbf{v}_1 \mathrm{d}\mathbf{v}_2 = E_f n_1 n_2 < \sigma v > \tag{1.5}$$

where $|\mathbf{v}_1 - \mathbf{v}_2|$ is the relative speed of the particles and $< \sigma v >$ is the velocity averaged cross-section. The velocity averaged cross-sections for $D - D$,D_T and $D - {}_2He^3$ are displayed in fig. 1.4. It shows that for whole plotted range of temperatures the $D - T$ reaction will have the highest reaction rates. Fusion reaction with energies released in

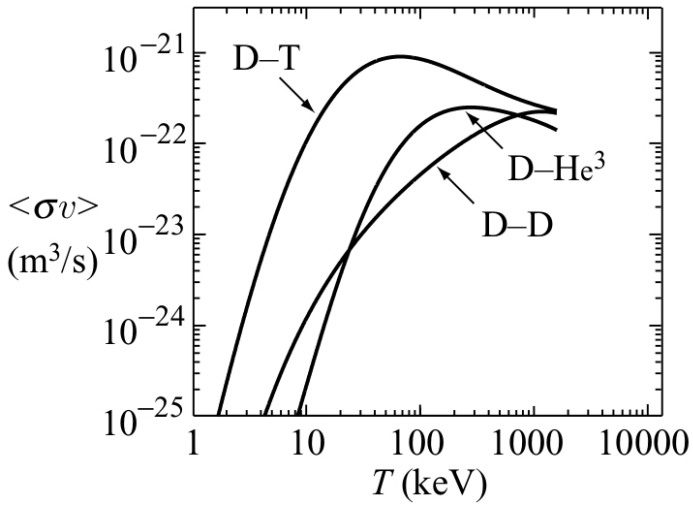

Figure 1.4: Velocity averaged fusion cross sections for $D - D$,$D - T$ and $D - {}_2He^3$ fusion reactions. Cross-sections are plotted as functions of temperature. Reprinted from [1].

a single fusion event are listed in eq. (1.6).

$$\begin{aligned} D + T &\rightarrow {}_2He^4 + n + 17.6MeV \\ D + D &\rightarrow {}_2He^3 + n + 3.27MeV \\ D + D &\rightarrow T + p + 4.03MeV \\ D + {}_2He^3 &\rightarrow {}_2He^4 + p + 18.3MeV \end{aligned} \tag{1.6}$$

Comparing the reaction rates and power densities of described fusion reactions of light elements clearly shows why the $D - T$ reaction is the most suitable candidate to be used in first fusion power plants. The reaction has the highest velocity averaged cross-section and its maximum occurs at temperatures close to 100keV. One disadvantage of the $D - T$ reaction is the production of high-energy neutrons. Presently, there is no way of confining neutrons produced in the reactor, which puts an additional load on reactor walls. Another disadvantage is the abundance of tritium on earth. Deuterium is naturally present on the Earth and can be gathered from sea water for example. Tritium is a radioactive isotope of hydrogen with half-time of 12.3 years. There is almost no natural source of tritium on the Earth and it will have to be manufactured. One way of obtaining tritium is production through reaction of lithium with neutron

[2]. Two reactions of lithium with neutrons resulting in production of tritium are listed below

$$\begin{aligned} {}_3Li^6 + n &\rightarrow {}_2He^4 + T + 4.8MeV \\ {}_3Li^7 + n &\rightarrow {}_2He^4 + T + n2.5MeV \end{aligned} \tag{1.7}$$

It is planned that tritium will be produced on-site in fusion power plants. Future reactors will be surrounded in blankets made of lithium, which will react with neutrons generated in the reactor in $D-T$ fusion process. The schematic of overall reaction planned to be used in first fusion power plants is shown in fig. 1.5

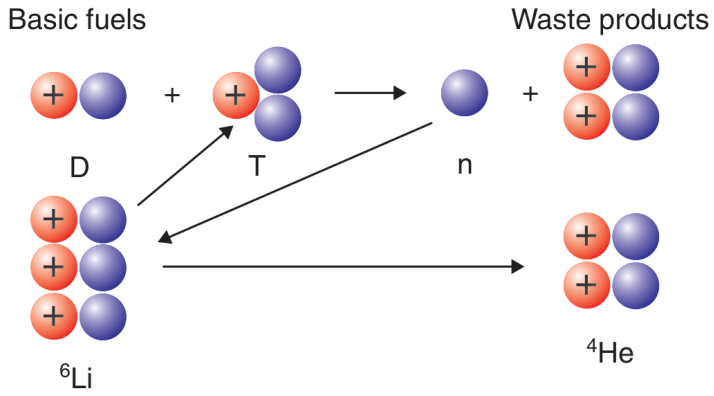

Figure 1.5: Schematic showing diagram of nuclear reaction planned to be used in first fusion nuclear plants. The fuel is lithium and deuterium. The waste product is helium. Reprinted from [2].

1.2 Confinement

It was shown in previous section that it is sufficient to accelerate particles to energies of tens of keV to initiate fusion reactions between deuterium and tritium. Such energies are easily achievable in laboratories. For example fusion reactions can be initiated by hitting a target made of tritium by a beam of accelerated deuterium. This elementary setup is suitable to measure fusion cross-sections for example, but not to generate energy. The reason is the size of the cross-section. Even at maximum values the cross-section is of the order of $\cdot 10^{-28} m^2$ for $D-T$ fusion. Only a very small fraction of accelerated particles will initiate fusion reaction. Majority of the particles will be scattered off the tritium target. The energy used to accelerate all the particles is higher than the energy generated by fusion reactions. One way how to achieve positive

energy balance with fusion is heating up particles to temperatures suitable for fusion reactions and confining them. Within such temperature range particles form a plasma. The level of ionization in the plasma depends on the temperature and species of ions. Light elements as isotopes of hydrogen and helium are in the form of bare particles within the range of temperatures suitable for fusion. The idea of confinement is to lower the rate of energy losses. If the confinement is good enough, confined particles will initiate enough fusion reactions to achieve the positive energy balance.

1.3 Magnetic Confinement

Magnetic confinement uses effects of Lorentz force acting on charged particles. Equation of motion for a charged particle in magnetic field is

$$m\frac{d\mathbf{v}}{dt} = q(\mathbf{v} \times \mathbf{B}) \tag{1.8}$$

where $m, \mathbf{v}, q, \mathbf{B}$ is particle mass, particle velocity and magnetic field, respectively. The cross product in eq. (1.8) shows that only components of velocity perpendicular to the magnetic field are influenced. Examining eq. (1.8) closely shows, why magnetic field can be used to confine carged particles. First thing to notice is the fact, that the kinetic energy of the particle is constant in time. This can be verified by taking a scalar product of eq. (1.8) with the particle velocity $\mathbf{v}$:

$$m\mathbf{v} \cdot \frac{d\mathbf{v}}{dt} = \frac{d}{dt}\frac{mv^2}{2} = q\mathbf{v} \cdot (\mathbf{v} \times \mathbf{B}) = 0 \tag{1.9}$$

The second thing to notice is the trajectory of the particle in the magnetic field $\mathbf{B}$. The solution of latter equation for static, uniform magnetic field can be separated into two components. Velocities parallel $\mathbf{v}_{\parallel}$ and perpendicular $\mathbf{v}_{\perp}$ to the $\mathbf{B}$. The $\mathbf{v}_{\parallel}$ component stays unaffected by $\mathbf{B}$ and the perpendicular components of velocity $\mathbf{v}_{\perp}$ result in a circular motion. Putting it all together shows, that charged particles in a magnetic field tend to follow magnetic field lines and their trajectories are helical. An example of the charged particle trajectory can be seen in fig. 1.6. Characterization of single particle trajectory gets more complicated in non-uniform and non-static magnetic fields or in presence of other forces. In such case the trajectory of a particle does not have to be strictly circular in the plane perpendicular to $\mathbf{B}$ and particle drifts have to be taken into account. Single particle motion is thoroughly described for example in [3, 4]. For sake of this introduction the fact that charged particles tend to follow magnetic field lines is sufficient enough. The effect of a magnetic field on trajectories of charged particles is used in magnetic confinement. Charged particles will be confined

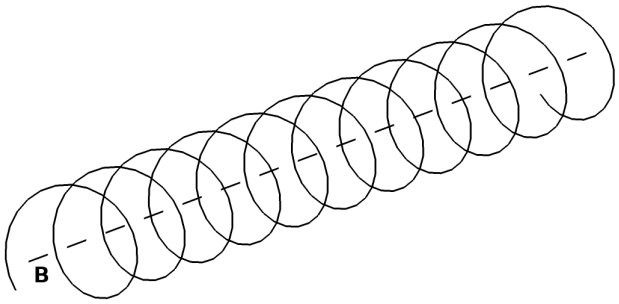

Figure 1.6: Helical trajectory of a charged particle in a static, uniform magnetic field **B**.

if exposed to a magnetic filed with field lines closing upon themselves. One example of such geometry of **B** is shown in fig. 1.7. The field lines of **B** have toroidal helical shape. In this configuration particles follow magnetic filed lines and are confined in the toroid. This lowers energy losses and allows the confined plasma to be heated to temperatures suitable for fusion without damaging the walls of the vacuum vessel. This configuration of magnetic field is used in tokamaks.

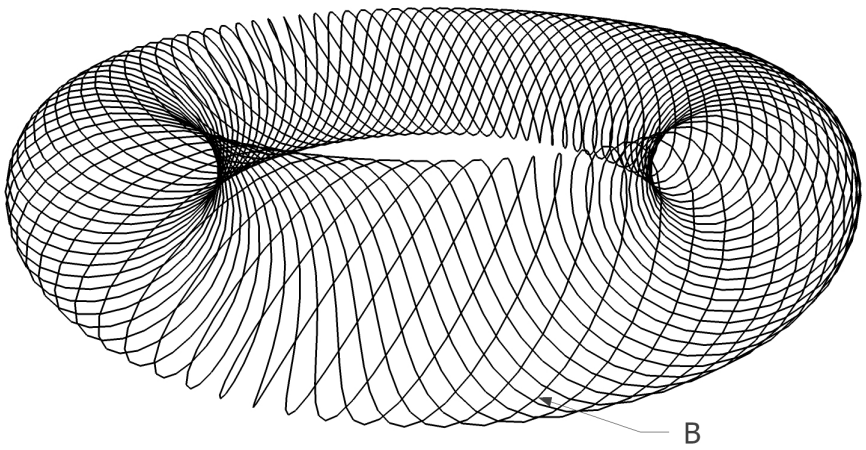

Figure 1.7: Scheme of toroidal helical field lines of magnetic field **B** in a Tokamak reactor.

1.4 Power Balance

The power balance is a sum of all mechanisms heating up the fusion plasma and energy losses mechanisms which are responsible for plasma cooling. The power balance equation can be derived from the equation for energy conservation [1]:

$$\frac{2}{3}\frac{\partial p}{\partial t} + \frac{3}{2}\nabla \cdot p\mathbf{v}p\nabla \cdot \mathbf{v} + \nabla \cdot \mathbf{q} = S \tag{1.10}$$

where the first term on the right represents the change of internal energy density, the second therm describes the net flux of energy density from the plasma volume and the third term denotes the energy losses due to expansion. The fourth term describes energy losses due to diffusive processes and the term on the left hand side is a sum of all energy sinks and sources. The term S from eq. (1.10) can be written as a sum:

$$S = S_f - S_r + S_h \tag{1.11}$$

where the S_f describes the heating delivered by fusion reactions, S_h stands for the energy input into the plasma by external heating systems and S_r describes radiation losses. The radiation losses are of the main interest in this work. The losses caused by generation of x-rays in the plasma are one of the main mechanisms of plasma cooling. There are three main contributors to the radiation. The free-free radiation or sometimes called breaking radiation or bremsstrahlung is generated during charged particle collisions . The power radiated by this mechanism can not be lowered or influenced. The second contributor is line radiation. It is generated by heavy atoms present in the plasma. For atoms like tungsten it becomes the main source of radiation losses. The last contribution is generated during radiative recombination of electrons with ions.

1.5 TOKAMAK

Tokamak is a device using magnetic field for plasma confinement. As said earlier, magnetic field lines have shape of a toroidal helix. A simple toroidal shape of magnetic field lines does not provide a good confinement . The reason is a charge separation being induced in plasma by particle drifts caused by non-isotropic curved $\mathbf{B}$ and gravity. This is removed in by introducing the poloidal component of $\mathbf{B}$ [5]. A scheme of tokamak reactor with circular vacuum vessel is displayed in fig. 1.10. The heated plasma is stored in a toroidal vacuum vessel. The plasma itself acts as a secondary winding in a transformer. Direct toroidal current is being driven in the plasma by gradually increasing current in the primary winding, which creates the poloidal component of

the magnetic field. The toroidal component of the magnetic field is created by toroidal coils. The way of generating poloidal magnetic field forbids tokamaks to be operated continuously. For the direct current to be driven in the plasma, the current in the primary winding has to be monotonically increasing. This can not be done infinitely. The pulse lengths can vary from fractions of seconds to minutes.

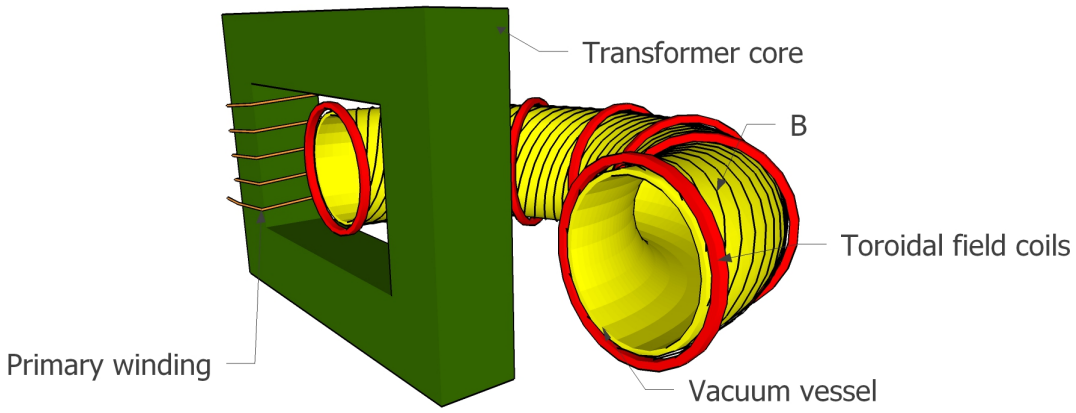

Figure 1.8: Scheme of a TOKAMAK with circular cross section.

1.6 Joint European Torus

JET (Joint European Torus) is built in Culham (United Kingdom) and is in operation since 1983. It is the largest tokamak in operation in the world today. The vacuum vessel of JET has the major radius 3 m, minor radius 0.9 m and has a D-shaped cross section. The volume of the vessel is $200m^3$. The inner wall of the vessel was recently changed, to allow testing of materials planned to be used in the ITER device. Currently the inner side of the vessel facing the plasma is made of beryllium and tungsten. Parts of JET inner wall which are not to be in a frequent contact with plasma are made of beryllium. It is a light element with atomic number 4. Atoms of beryllium are stripped of all electrons in the fusion plasma and their contribution to the energy losses are negligible when compared to elements with high atomic numbers. Tungsten is a hard metal with the highest melting point of all chemical elements. This is the reason why it is used for parts of the reactor wall which is predicted to have the most contact with the hot plasma. Although tungsten has a very high melting point, it is impossible to prevent tungsten atoms from entering the plasma. This can happen when the plasma touches the wall and sputters atoms of the wall material. These atoms are

then ionized and confined in the plasma and are in general called impurities. Tungsten ions aren't ionized into the state of bare nuclei even in the hottest parts of the plasma and their contribution to the radiation is very high. This causes decrease in the quality of the confinement. It will be described later in this work that the higher the atomic number of an element the higher radiation losses are caused. This is the reason why only parts of the rector wall are made of tungsten. It also explains the need of a way of investigating of distribution of tungsten atoms inside the plasma. A very convenient method allowing this is soft x-ray tomography. Facts about JET can be seen in tab. 1.2 or found at [6].

Volume	$200m^3$ - vessel, $80m^3$ plasma
Temperature	up to $\approx 20keV$
Plasma current	$5mA$
Magnetic field strength	$3.5T$
Ohmic heating	$4MW$
LHCD heating	$3MW$
ICRH hrating	$8MW$
Pressure peak	$2 \cdot 10^{-5}mbar$

Table 1.2: Specifications of JET, taken from [6].

1.7 Hot Plasma Tomography

Tomography in general is an ensemble of methods allowing determination of structure of an object from its observed projections. if the structure of an object can be described by a scalar function $g(\mathbf{r})$ where $\mathbf{r}$ is position vector. The corresponding projections onto the projection plane are given by $f(\mathbf{p})$. The projection function is given by:

$$f(\mathbf{p}) = \int g(\mathbf{r})\delta(p - \mathbf{r} \cdot \mathbf{n}) \tag{1.12}$$

where δ is Dirac delta function and $\mathbf{n} = \mathbf{p}/|\mathbf{p}|$ is a vector tangent to the projection plane. The inverse Radon transformation allows analytical determination of $g(\mathbf{r})$ from the function $f(\mathbf{p})$. In 2 dimensions :

$$g(\mathbf{r}) = \frac{1}{8\pi^2} \int\limits_{|\mathbf{n}|=1} \mathrm{d}\mathbf{n} v.p. \int\limits_{-\infty}^{\infty} \frac{1}{\mathbf{r} \cdot \mathbf{n}} \frac{\partial}{\partial p} f(\mathbf{p}) \mathrm{d}p \tag{1.13}$$

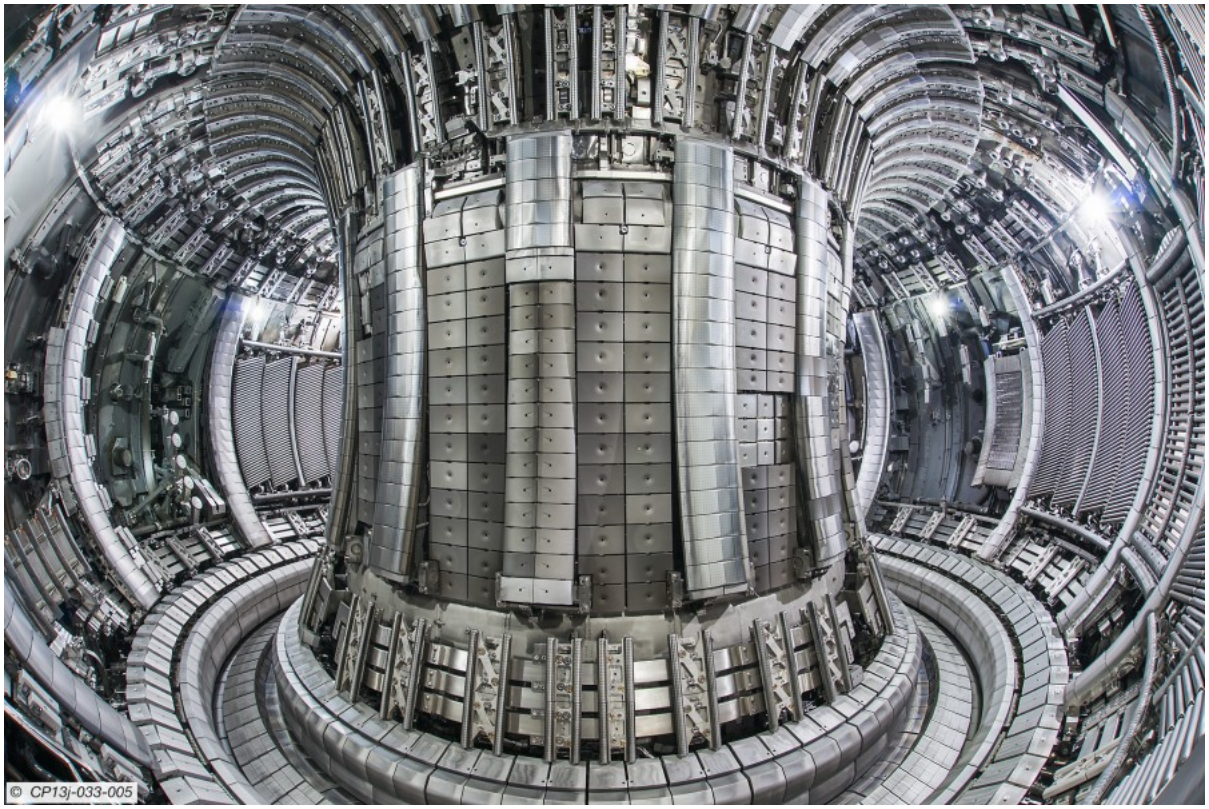

Figure 1.9: Internal view of the JET vessel after the 2012-13 maintenance.Reprinted from [6].

Radon transformation is an ill-conditioned problem. Discretization of the problem may introduce more than one solution and even small errors in measured data can cause high errors in the result called artifacts. This can be partly removed by introducing requirements for the result as maximal smoothness of the result or boundary conditions. Hot plasma tomography differs from regular commercially used tomography, in which projections in all directions are known. In case of fusion reactors projections can be measured only from limited number of directions determined by construction of the device. For example at JET, projections are measured only in two directions. This introduces difficulties in solving the inverse Radon transformation. In the case of the hot plasma tomography the reconstruction of the cross-section is discretized and the is given by a sum of basis functions:

$$g_i = \sum_{j}^{\infty} g_j b_j(\mathbf{r}) \tag{1.14}$$

The solution of the solution is then sought as a combination of finite sum of amplitudes of basis function which is optimal for measured data f_i:

$$f_i \doteq \sum_{j}^{N} T_{ij} g_j \quad i \in 1, 2, \ldots, N \tag{1.15}$$

Very convenient is the method of pixels, where the studied cross-section is separated into finite number of rectangles [7]. The simplest case of basis function becomes a function with value $b_j = 1$ in the pixel j and 0 elsewhere. Each element of the matrix of contributions T_{ij} in method of pixels expresses the contribution of a pixel j to the overall intensity in a chord i.

1.7.1 2D tomography of Soft X-ray data on JET

The setup for soft x-rays measurements of JET consists of three pinhole cameras which are installed in three different toroidal positions. The toroidal positions and the poloidal orientations of the cameras are displayed in fig. 1.10. Because of toroidal separation the plasma cross-section is considered to be constant in the toroidal direction. Currently the soft x-ray data are measured by horizontally oriented camera S4 (which will be call horizontal camera or H-camera from now on) and the vertically oriented camera V (which will be from now on called horizontal camera or H-camera). The thickness of the beryllium wall separating the cameras is different for H-camera and V-camera. The reasons are constrains given by the construction of the reactor vessel. The thickness of the wall is $250\mu m$ and $350\mu m$ for V-camera and H-camera, respectively. The difference in the thickness of the beryllium wall causes differences in measured intensities. This is due to fact that the beryllium acts as a filter, with spectral characteristics given by the thickness. This introduces errors in tomographic reconstructions and has to be delt with in order to achieve higher precisions of tomography results. More information about tomography system used on JET can be found in [8, 9].

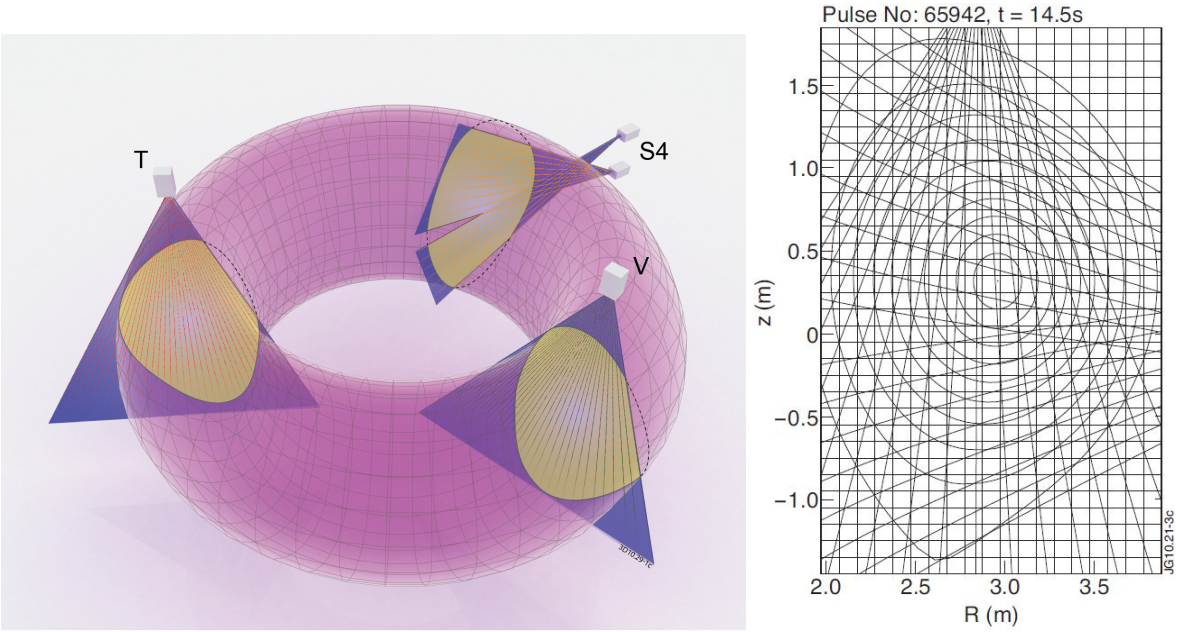

Figure 1.10: Positions of the soft x-ray cameras on JET. Courtesy of Assoc. Prof. Jan Mlynář.

Chapter 2

Atomic Processes in Hot Plasmas

X-ray radiation generated by hot plasma has its origins in electromagnetic interactions of charged particles and quantum-mechanical processes in ion orbitals. In order to create a model which can provide approximations of spectral power density of the x-ray radiation a brief knowledge of atomic structure, atomic processes and at last distribution of ionic states in plasma is required. In the first part of this chapter a brief theoretical background of atomic structure is given together with basic desctiption of atomic processes, in which energies and charges of ions are changed. In the second part, basic models allowing for an estimation of the distribution of ionic states in plasma are given.

2.1 Atomic Structure

The first step towards understanding the structure of an atom was made by Rutherford who proposed that atoms consist of a positively charged nucleus which carries most of the mass of an atom. According to Rutherford the nucleus is surrounded by an electron shell, in which electrons orbit around the nucleus on elliptic or circular trajectories. The above described atomic model was in agreement with measurements of alpha particle scattering by heavy nuclei, but in contrary with the electromagnetic field theory. It can be derived from the laws of electromagnetics, that accelerated charged particles emit electromagnetic radiation. If this phenomena is applied to the case of an electron orbiting a nucleus, the electron should radiate its kinetic energy in form of an electromagnetic radiation and fall into the nucleus in the order of 10^{-8}s. Rutherford's model is also in disagreement with spectral properties of radiation generated by atoms. Contrary to accelerated charge emitting radiation with continuous spectrum, spectra generated by atoms consist of separated spectral lines. These contradictions

were solved by Bohr who proposed that electrons bound to an atom can assume only steady states with discrete sets of energies. In these particular states, electrons do not emit any electromagnetic radiation. The only event in which electromagnetic radiation is generated is a transition of an electron between two steady states with different energies, during which a photon is emitted. The energy of the emitted photon corresponds to the energy difference of the initial and the final state $E = E_i - E_f$, where E_i and E_f are the energies of the electron in the initial and the final state, respectively. The Bohr model of atoms was further developed by principles of quantum mechanics. Descriptions of electron energies and orbitals using principal, orbital and magnetic quantum numbers were introduced.

2.1.1 Electron Orbitals

The description of electron orbitals using quantum numbers rises from the solution of the time independent Schrödinger equation in polar coordinates:

$$\left[-\frac{h^2}{2m_e}\nabla^2 + V(\mathbf{r})\right]\Psi(\mathbf{r}) = E\Psi(\mathbf{r}) \tag{2.1}$$

where Ψ is the wave function, E is energy of the system, V is the potential, ∇ is the Hamiltonian operator and m_e is mass of an electron. Analytical solutions of eq. (2.1) are possible only for simple systems, e.g. for hydrogen atoms. The solution of eq. (2.1) for a hydrogen atom is given in [10]. Introducing functions for motion in separate spatial dimensions $\Psi(\mathbf{r}) = R(r)\Theta(\theta)\Phi(\phi)$ in polar coordinates and separating gives a set of three equations describing azimuthal, polar and radial motion of the electron. The solution of the azimuthal equation introduces a magnetic quantum number m_ℓ which must be an integer. The magnetic quantum number m_ℓ determines one component of angular momentum $L_z = m_\ell\hbar$ (where the z coordinate was chosen arbitrarily).

$$m_\ell = 0, \pm1, \pm2, \pm3, \ldots \quad , \quad L_z = m_\ell\hbar \tag{2.2}$$

The solution of the polar equation introduces quantization of magnitude of the angular momentum $|\mathbf{L}| = \sqrt{\ell(\ell+1)}\hbar$. The orbital quantum number ℓ can only be a non-negative integer. Because $L_z < |\mathbf{L}|$ the angular momentum gives a restriction for values of m_ℓ.

$$\begin{array}{lll} \ell = 0, 1, 2, 3 \ldots & , & |\mathbf{L}| = \sqrt{(\ell(\ell+1)}\hbar) \\ m_\ell = 0, \pm1, \pm2, \pm3, \ldots, \pm\ell & , & L_z = m_\ell\hbar \end{array} \tag{2.3}$$

Solutions of the radial equation yields a principal quantum number n, which introduces quantization of the electron's energy. As magnitude of angular momentum is connected to the energy of the particle and described by the angular quantum number ℓ, the

principal quantum number puts a restriction on the orbital quantum number: $\ell \leq n-1$. The system of orbital quantum numbers describing a single electron orbital is then:

$$\begin{array}{lll} \ell = 0, 1, 2, 3 \ldots, n-1 & , & |\mathbf{L}| = \sqrt{(\ell(\ell+1)}\hbar) \\ m_\ell = 0, \pm 1, \pm 2, \pm 3, \ldots, \pm \ell & , & L_z = m_\ell \hbar \end{array} \tag{2.4}$$

The last quantum number determining the electron state is a quantum number m_s. It specifies the spin state of the electron (rising from magnetic dipole moment and angular momentum of an electron, its intrinsic properties). The electron spin quantum number can only take values $m_s = \pm 1/2$. The state of an electron in an atom orbital is described by three quantum numbers: n, ℓ, m_ℓ, specifying the electron's spatial state and spin quantum number m_s, specifying electron's spin state. The system of quantum numbers describing an electron state is given in eq. (2.5).

$$\begin{array}{lll} \ell = 0, 1, 2, 3 \ldots, n-1 & , & |\mathbf{L}| = \sqrt{(\ell(\ell+1)}\hbar) \\ m_\ell = 0, \pm 1, \pm 2, \pm 3, \ldots, \pm \ell & , & L_z = m_\ell \hbar \\ m_s = \pm \frac{1}{2} & & \end{array} \tag{2.5}$$

2.1.2 Energy Levels of an Atom

The potential energy term $V(\mathbf{r})$ in eq. (2.1) has only a radial dependence for an atom with a single electron and the wavefunction Ψ can be obtained analytically. The problem however becomes complicated for atoms with multiple electrons, because the potential energy term becomes a function of all three spatial variables. This is due to fact that electrons bound to atom influence each other via electric field. This influence is taken into account in [11], where the solution of a wave function depends on position $\mathbf{R}$ and on position of all other electrons $\mathbf{r}'$.

$$\left[-\frac{h^2}{2m_e}\nabla^2 + V(\mathbf{r}) + \sum_{j,j\neq i} e^2 \int \frac{\Psi_j^*(\mathbf{r}')\Psi_i(\mathbf{r})}{|\mathbf{r}' - \mathbf{r}|} d\mathbf{r}' \right] \Psi_i(\mathbf{r}) = E_i \Psi(\mathbf{r}) \tag{2.6}$$

Exact solutions of wave functions Ψ of electrons in multi-electron atom are impossible to obtain, only approximative solutions are available. Electrons occupying orbitals in atoms follow Pauli exclusion principle. The principle says that two electrons in an atom can not be in the same energy state. This implies that two electrons in an orbital can not be described by the same set of quantum numbers, it has to differ at least in one number.Electrons also tend to fill orbitals to form a ground state atom. Electrons in ground state atoms form configurations of orbitals for which the overall energy of the atom is the lowest possible. Only approximative energies of orbitals are available, but a following rule of thumb, which is in a good agreement with experiments, can be used to estimate which orbitals in a ground state atom are occupied. Electrons

occupy orbitals from lowest $n+\ell$. In in case of equal $n+\ell$, lower n always gives lower energy. This is a way to separate electron orbitals into shells denoted by principal quantum number n and sub-shells denoted by $n\ell$. In tab. 2.1 number of electrons in each sub-shell is shown. A metastable or excited state of an atom is a state in which

subshell $n\ell$	1s	2s	2p	3s	3p	4s	3d	4p	5s	4d	5p	6s	4f	5d	6p
$n+\ell$	1	2	3	3	4	4	5	5	5	6	6	6	7	7	7
number of electrons $2(2\ell+1)$	2	2	6	2	6	2	10	6	2	10	6	2	14	10	6

Table 2.1: Summary of electron orbitals with number of electrons in each sub-shell.

overall energy is not minimized. Due to various atomic processes, an electron in an inner orbital can absorb energy ΔE. As a result of this absorption, the electron jumps to a state with higher energy $E_f = E_i + \Delta E$. The atom or ion is in an excited state with a vacancy in an inner shell. The energy of the atom is not the lowest possible.

2.2 Atomic Processes

Photons, electrons and ions in hot plasma interact with each other via their electromagnetic properties. Charged particles undergo collisions during which they act on each other via Coulomb fore. Collisions can effect energy states of states of colliding particles, leading to changes of distribution of states in plasma. Such changes have a direct influence on spectral properties of x-ray radiation generated in plasma. In this section a brief description of atomic processes is given. Electron-electron and ion-ion interactions will be omitted in this text, due to their lower significance. The reason is that electron-electron collisions do not have any direct impact on spectral properties of radiation generated by plasma. The frequency of ion-ion collisions is much smaller than the frequency of electron-ion collisions and although ion-ion collisions can change ionic states, the rates of changes are insignificant compared to rates of electron-ion collisions.

2.2.1 Spontaneous Decay & Resonant Photoabsorbtion

Spontaneous decay is a process, in which an ion in an initial excited state with energy E_i decays into a final state with lower energy E_f. The energy state E_f does not have to be the ground state. The difference in energies $\Delta E = E_i - E_f$ is radiated in a form of a photon with the frequency $\nu = E/h$. The opposite process of Spontaneous decay is resonant photoabsorption. A process in which electron jumps into an orbital

with higher energy after absorption of a photon. The absorbed or radiated photons have energy equal to the energy difference between orbitals, which is unique to every element. This uniqueness of spectra can be used to determine presence of elements in the plasma by examining line radiation or line vacancy.

$$A_{\zeta,m} + h\nu \Leftrightarrow A_{\zeta,m'} \tag{2.7}$$

2.2.2 Electron Impact Ionization & Three Body Recombination

When a free electron collides with an atom or an ion, it can transfer part of its kinetic energy to a bound electron. If the transferred energy is higher than the ionization energy of the bound electron, the bound electron is knocked from the orbital into the continuum. This process is called electron impact ionization, in which the charge state of an atom is increased by 1. An opposite process is called three body recombination. It can occur only when two free electrons are interacting with an ion at the same time. In this case one of the colliding electrons can become bounded and the difference in energy is transferred to the second colliding electron. The second electron remains free and gains kinetic energy equal to the energy released during the recombination. The rate of three body recombination process is proportional to square of electron density and compared to rates of other processes can be neglected for low density plasma. The three body recombination process gains importance with growing plasma density and has to be taken into account for plasma in local thermal equilibrium.

$$A_{\zeta,m} + e \Leftrightarrow A_{\zeta+1,m'} + e + e \tag{2.8}$$

2.2.3 Electron Impact Excitation & Deexcitation

The electron impact excitation is a process similar to electron impact ionization. A free electron interacts with one of the bound electrons, during collision with ion or atom. During the interaction, it transfers part of is kinetic energy ΔE and the bound electron is excited from an initial bound state E_i to final bound state $E_f = E_i + \Delta_i$ and the energy state of an ion is changed. Electron impact deexcitation is a process in which free electron gains kinetic energy in a collision with an excited atom or an ion. The transferred energy is released by a bound electron, which decays to an orbital with lower energy.

$$A_{\zeta,m} + e \Leftrightarrow A_{\zeta,m'} + e \tag{2.9}$$

2.2.4 Photoionization & Radiative Recombination

Another process in which a photon is absorbed by a bound electron is Photoinisation. In this case the energy $E = h\nu$ carried by the photon is higher than the ionization energy of the interacting electron. The electron becomes free, increasing the charge number of the ion by one. The opposite process is radiative recombination. A free electron becomes bound after radiating a photon during an interaction with an ion. The frequency of the radiated photon depends on the kinetic energy of the electron before recombination and on the energy of the orbital occupied by the electron in the atom.

$$A_{\zeta,m} + e \Leftrightarrow A_{\zeta+1,m'} + h\nu \tag{2.10}$$

2.2.5 Autoionization & Dielectronic Recombination

This group of processes involves doubly excited ions or atoms. A doubly excited ion or atom has two vacancies in lower shells. During an autoionization one of the excited electrons decays to the ground state and the difference in energies is transferred to the second excited electron, which is knocked out of the orbital into the continuum. The process of Dielectronic recombination includes two steps. In the first step, a free electron recombines into an excited state in an ion and transfers the energy released during recombination to a electron bound to the atom, which becomes excited. In the second step the ion undergoes a radiative stabilization when one of the excited electrons decays (the probability of decay of the electron with lower energy is higher) into a ground state. The energy difference is radiated as a photon.

$$A_{\zeta+1,m} + e \Leftrightarrow A_{\zeta,m''} \rightarrow A_{\zeta,m'} + h\nu \tag{2.11}$$

2.3 Plasma Models

The shape of the spectral power density of x-ray radiation generated by hot plasma is determined by atomic processes and particle interactions taking place in plasma. The rate of contribution of a process to the intensity of x-ray radiation produced in a volume of plasma is dependent on the probability of the process and the density of the interacting particles. by using the probability of atomic processes, sets of equations can be composed and solved to obtain the distribution function of ionic states. These sets of equations can be simplified by accepting plasma models, which neglect atomic processes with low probabilities, certain energy states of ions or by use laws of statistical thermodynamics. In this sections, such models for plasma are described.

2.3.1 Local Thermal Equilibrium

Plasma is considered to be in Local Thermal Equilibrium (LTE) when its characteristic dimensions are significantly smaller than the mean free path of photons but larger than the mean free path of electrons and ions. This implies that photons emitted in the LTE region escape without interacting with other particles and are not necessarily in an equilibrium with other particles. Ions and electrons collide frequently in the LTE region and their velocity distributions tend to follow the Maxwell-Boltzmann velocity distribution. The LTE model is valid for plasma, in which rates of collisional processes dominate over rates of radiative processes. A rule-of-thumb for latter condition is given in [12] and is:

$$n_e >> 10^{19}\sqrt{T}\Delta E^3 m^{-3} \tag{2.12}$$

where T and ΔE are plasma temperature and energy difference of the ionic state before and after the process in eV, respectively. Evaluating the equation for hydrogen plasma with temperature $T = 1.5keV$ gives the requirement for the electron plasma density to be higher than $1.5 \cdot 10^{24} m^{-3}$. Such conditions are achieved very rarely even in magnetic fusion plasma.

2.3.2 Corona Equilibrium

Corona Equilibrium applies to very low density, optically thin plasmas in which all excitation processes are strictly collisional and deexcitation processes are only radiative. According to [13] it can be assumed that all ions are in ground states:

$$P_\zeta, m = \begin{cases} 1 & \text{ground state} \\ 0 & \text{exited states} \end{cases} \tag{2.13}$$

This assumption can be made comparing rates of ion excitation to life times of excited states. Due to low density of plasma, an excited atom is most likely to spontaneously decay to the ground state before being excited again. Another safe assumption is neglecting three body recombinations due to low plasma density. The distribution of charged states is then guided by the electron impact ionization, the radiative recombination and the dielectronic recombination. The LTE is considered a steady state of plasma, which implies that rates of processes populating and depopulating an atomic must equal.

$$n_e N_{\zeta-1} \mathcal{I}\left(\zeta - 1 \to \zeta; T_e\right) = n_e N_\zeta \left[\mathcal{R}^{(\mathrm{r})}\left(\zeta \to \zeta - 1; T_e\right) + \mathcal{R}^{(\mathrm{d})}\left(\zeta \to \zeta - 1; T_e\right)\right] \tag{2.14}$$

$$N = n_e \tag{2.15}$$

$$N = \sum_\zeta N_{\zeta,0} \tag{2.16}$$

Constructing eq. (2.14) for all charge states gives a set of Z+1 linear coupled equations. Adding eq. (2.15) for plasma neutrality and eq. (2.14) for all charge states forms a set of equations, which can be solved in order to obtain the distribution of ion charge states. It is interesting to notice that the distribution of charge states is independent of the electron density n_e. It is governed only by rate coefficients which are functions of temperature. Another interesting point arises, when reaction rates of the energy conserving processes are compared with reaction rates of energy dissipative processes, which are much more frequent in the corona equilibrium. The result shows that plasma in corona equilibrium is not a factual equilibrium state. Due to frequent radiative recombination of electrons, plasma in corona equilibrium without external heating cools down in time. If the external heating is applied, the plasma is in a steady state.

2.3.3 The Collisional Radiative Steady State

In the Collisional Radiative Steady State (CRSS) ions interacting with other particles can assume any state ζ, m. The ion charge ζ can go from $\zeta = 0$ for neutral atom to totally ionized ion $\zeta = \mathrm{Z}$. The excitation state m can assume any value from ground state $m = 0$ to the highest energy state $m = M_\zeta$. The equation giving the ion concentration is then:

$$N = \sum_{\zeta=0}^{Z} \sum_{m=0}^{M_\zeta} N_{\zeta,m} \tag{2.17}$$

The rates of processes changing the ion state from ζ, m to ζ', m' can be set equal to the rates of processes changing the ion state from ζ', m' to ζ, m. This is due to the fact that the plasma is considered to be in a steady state. According to [13], the equation giving the relation between densities of states ζ, m and ζ', m' is:

$$\sum_{\substack{populating \\ processes}} n_e^k N_{\zeta',m'} \mathcal{R}\left(\zeta', m' \to \zeta, m; T_e\right) = \sum_{\substack{depopulating \\ processes}} n_e^k N_{\zeta',m'} \mathcal{R}\left(\zeta, m \to \zeta', m'; T_e\right)$$
$$\zeta = 0, 1, \ldots Z \qquad \zeta' = \zeta, \zeta \pm 1 \qquad m, m' = 0, 1, \ldots, M_{\zeta'} \tag{2.18}$$

where $\mathcal{R}$ is the rate coefficient of process in $cm^{3k}s^{-1}$ and k is the number of electrons interacting in the process. Plasma in CRSS is assumed to be optically thin. After neglecting resonant photon absorption, there are seven processes populating and depopulating ion states:

- Spontaneous decay with rate coefficient given by the Einstein coefficient $\mathcal{A}$.

- Electron impact ionization, excitation and deexcitation with rate coefficients $\mathcal{I}$,$\mathcal{E}$ and $\mathcal{D}$, respectively.

- Radiative, dielectronic and three-body recombination with rate coefficients $\mathcal{R}^{(r)}$, $\mathcal{R}^{(d)}$ and $\mathcal{R}^{(3)}$, respectively.

Finding the ion distribution by solving the set of equations given by eq. (2.18) becomes a challenging problem. It can be seen in eq. (2.19) where eq. (2.18) is rewritten, including all atomic processes for the ion state (ζ, m).

$$
\begin{aligned}
&N_{\zeta,m} \sum_{m'<m} \mathcal{A}\left(\zeta, m \to \zeta, m'\right) + n_e N_{\zeta,m} \Bigg\{ \sum_{m'} \mathcal{I}\left(\zeta, m \to \zeta+1, m'; T_e\right) + \\
&+ \sum_{m'} \left[\mathcal{R}^r\left(\zeta, m \to \zeta-1, m'; T_e\right) + \mathcal{R}^d\left(\zeta, m \to \zeta-1, m'; T_e\right) \right] + \\
&+ \sum_{m'>m} \mathcal{E}\left(\zeta, m \to \zeta-1, m'; T_e\right) + \sum_{m'<m} \mathcal{D}\left(\zeta, m \to \zeta, m'; T_e\right) \Bigg\} + \\
&+ n_e^2 N_{\zeta,m} \sum_{m'} \mathcal{R}^3\left(\zeta, m \to \zeta-1, m'; T_e\right) = \\
&= \sum_{m'>m} N_{\zeta,m'} \mathcal{A}\left(\zeta, m' \to \zeta, m\right) + n_e \Bigg\{ \sum_{m'} N_{\zeta-1,m'} \mathcal{I}\left(\zeta-1, m' \to \zeta, m; T_e\right) + \\
&+ \sum_{m'} N_{\zeta+1,m'} \left[\mathcal{R}^r\left(\zeta+1, m' \to \zeta, m; T_e\right) + \mathcal{R}^d\left(\zeta+1, m' \to \zeta, m; T_e\right) \right] + \\
&+ \sum_{m'>m} N_{\zeta,m'} \mathcal{E}\left(\zeta, m' \to \zeta, m; T_e\right) + \sum_{m'<m} N_{\zeta,m'} \mathcal{D}\left(\zeta, m' \to \zeta, m; T_e\right) \Bigg\} + \\
&+ n_e^2 \sum_{m'} N_{\zeta-1,m'} \mathcal{R}^3\left(\zeta-1, m' \to \zeta, m; T_e\right) \\
&\qquad \zeta = 0, 1, \ldots, Z \qquad m = 0, 1, \ldots, M_\zeta
\end{aligned}
\tag{2.19}
$$

2.3.4 Low Density Plasmas

A set of approximations for low density plasmas suggested in [13] allows simplification of eq. (2.19). The first simplification is done by neglecting terms including process of three body recombination in eq. (2.19). This is justified for low density plasma. The reason is that the three body recombination process scales with n_e^2 and the rate in low density plasma is negligible compared to other atomic processes. Another simplification of eq. (2.19) can be made by taking the assumption that the probability distribution of

ionic states is very close to Corona Equilibrium eq. (2.13). The density of excited ionic states is very low, almost zero. This allows for the assumption that initial states of ions in eq. (2.19) are ground states. The first term on the right hand side gives the reaction rate of spontaneous decay between two excited states. It can be neglected together with the sixth term on the right hand side which gives the reaction rate of electron impact deexcitation. Replacing the partial densities of excited states with population probabilities $N_{\zeta,m} = N_\zeta P(\zeta, m)$, dividing the equation by n_ζ and using all the latter approximations, the equation eq. (2.19) for an excited state $m \neq 0$ can be rewritten as:

$$\begin{aligned}
&P(\zeta,m)\sum_{m'<m}\mathcal{A}(\zeta,m\to\zeta,m')+n_eP(\zeta,m)\left\{\sum_{m'}\mathcal{I}(\zeta,m\to\zeta+1,m';T_e)+\right.\\
&+\sum_{m'}\left[\mathcal{R}^{(r)}(\zeta,m\to\zeta-1,m';T_e)+\mathcal{R}^{(d)}(\zeta,m\to\zeta-1,m';T_e)\right]+\\
&\left.+\sum_{m'>m}\mathcal{E}(\zeta,m\to\zeta-1,m';T_e)+\sum_{m'<m}\mathcal{D}(\zeta,m\to\zeta,m';T_e)\right\}=\\
&=n_e\left\{\frac{N_{\zeta-1}}{N_\zeta}\mathcal{I}(\zeta-1,0\to\zeta,m;T_e)+\mathcal{E}(\zeta,0\to\zeta,m;T_e)+\right.\\
&\left.+\frac{N_{\zeta+1}}{N_\zeta}\left[\mathcal{R}^{(r)}(\zeta+1,0\to\zeta,m;T_e)+\mathcal{R}^{(d)}(\zeta+1,0\to\zeta,m;T_e)\right]\right\}\\
&\qquad\zeta=0,1,\ldots,Z\qquad m=1,2,\ldots,M_\zeta
\end{aligned}\tag{2.20}$$

The latter equation can be solved for the population probability $P(\zeta, m)$, which is a function of electron density and temperature through the rate coefficients. Because the plasma density is assumed to be low, the ratios of the adjacent ionic ground states $N_{\zeta-1}/N_\zeta$ and $N_{\zeta+1}/N_\zeta$ can be obtained from the equation for Corona Equilibrium eq. (2.14):

$$\frac{N_{\zeta-1,0}}{N_{\zeta,0}}=\frac{\sum_{m'}\left[\mathcal{R}^{(r)}(\zeta,0\to\zeta-1,m';T_e)+\mathcal{R}^{(d)}(\zeta,0\to\zeta-1,m';T_e)\right]}{\sum_{m'}\mathcal{I}(\zeta-1,0\to\zeta,m';T_e)}\tag{2.21}$$

where the following equalities were assumed

$$\begin{aligned}
\mathcal{R}^x(\zeta,0\to\zeta-1;T_e)&=\sum_{m'}\mathcal{R}^x(\zeta,0\to\zeta-1,m';T_e)\\
\mathcal{I}(\zeta,0\to\zeta+1;T_e)&=\sum_{m'}\mathcal{I}(\zeta,0\to\zeta+1,m';T_e)
\end{aligned}\tag{2.22}$$

Plugging eq. (2.21) into eq. (2.20) and solving for population probability $P(\zeta, m)$ gives an equation of following shape:

$$P(\zeta, m) = \frac{n_e}{f_{\zeta,m}} \tag{2.23}$$

$$f_{\zeta,m} = \frac{A + Bn_e}{C} \tag{2.24}$$

where $m \neq 0$ and

$$A = \sum_{m'<m} \mathcal{A}(\zeta, m \to \zeta, m') \tag{2.25}$$

$$\begin{aligned} B = &\sum_{m'} \mathcal{I}(\zeta, m \to \zeta + 1, m'; T_e) + \sum_{m'>m} \mathcal{E}(\zeta, m \to \zeta - 1, m'; T_e) + \sum_{m'<m} \mathcal{D}(\zeta, m \to \zeta, m'; T_e) \\ &+ \sum_{m'} \left[\mathcal{R}^{(r)}(\zeta, m \to \zeta - 1, m'; T_e) + \mathcal{R}^{(d)}(\zeta, m \to \zeta - 1, m'; T_e)\right] \end{aligned} \tag{2.26}$$

$$\begin{aligned} C = &\mathcal{E}(\zeta, 0 \to \zeta, m; T_e) + \\ &+ \frac{\mathcal{I}(\zeta - 1, 0 \to \zeta, m; T_e) \sum_{m'} \left[\mathcal{R}^{(r)}(\zeta, 0 \to \zeta - 1, m'; T_e) + \mathcal{R}^{(d)}(\zeta, 0 \to \zeta - 1, m'; T_e)\right]}{\sum_{m'} \mathcal{I}(\zeta - 1, 0 \to \zeta, m'; T_e)} + \\ &+ \frac{\left[\mathcal{R}^{(r)}(\zeta, 0 \to \zeta - 1, m; T_e) + \mathcal{R}^{(d)}(\zeta, 0 \to \zeta - 1, m; T_e)\right] \sum_{m'} \mathcal{I}(\zeta - 1, 0 \to \zeta, m')}{\sum_{m'} \mathcal{I}(\zeta - 1, 0 \to \zeta, m'; T_e)} \end{aligned} \tag{2.27}$$

By using latter equation to estimate probabilities of all states $p_{\zeta,m\neq 0}$, the probability of ground states $P_{\zeta,0}$ can be obtained using:

$$P_{\zeta,0} = 1 - \sum_{m=1}^{M_\zeta} P(\zeta, m) \tag{2.28}$$

Chapter 3

X-Ray Radiation Generated in Hot Plasmas

X-ray radiation generated in a hot plasma can be separated into two groups by spectral properties. The first with continuous spectrum, produced by bremsstrahlung. Bremsstrahlung or breaking radiation can be separated into two cases. The first case called free-free radiation and the second case free-bound radiation. The second group has a line (discontinuous) spectrum generated by spontaneous decay of excited ion states. In this chapter all latter mechanisms of x-ray production are described, basic theoretical framework for spectral power density estimation is given and the importance of mechanisms in plasmas with different properties is discussed.

3.1 Free-free Radiation

The free-free radiation is generated during an electron-ion Coulomb collision. The reason is acceleration of the colliding electron. The energy radiated during the event is low enough for the electron to remain free after the interaction and is hence called free-free radiation. As claimed in [1, 14], the ion-ion collision frequency is much lower than the electron-ion collision frequency. In the case of electron-electron collisions, momenta of interacting particles are not changed and the contribution to the free-free radiation is zero. The contribution to free-free radiation from interactions of particles of the same species can therefore be omitted. As will become obvious at the end of this section, free-free radiation is the main or the only source of x-ray radiation in plasmas containing only fully ionized ions. In the following section a classical derivation of emissivity of free-free radiation generated by a Maxwellian plasma is provided. The errors made by classical treatment and approximations made during the derivation can

be corrected by given Gaunt factors.

3.1.1 Energy radiated during Single Electron-Ion Coulomb Collision

The power radiated by an accelerated particle is described by the Larmour formula eq. (3.1), providing a relation between radiated power P and acceleration $\dot{\mathbf{v}}$.

$$P = \frac{1}{4\pi\varepsilon_0}\frac{2e^2}{3c^3}|\dot{\mathbf{v}}|^2 \tag{3.1}$$

The energy spectrum radiated during an electron-ion Coulomb collision can be obtained via Fourier transform of eq. (3.1).

$$\frac{dE}{d\nu} = \frac{4e^2}{4\pi\varepsilon_0 3c^3}\left|\int_{-\infty}^{\infty}\dot{\mathbf{v}}\mathrm{e}^{i\omega t}\mathrm{d}t\right|^2 \tag{3.2}$$

The classical treatment of free-free radiation is provided in this text only. A more detailed analysis of the free-free radiation spectra, approximative solutions of eq. (3.2) and Gaunt factors are presented in [15, 12, 14]. A quantum mechanical treatment is necessary to correctly characterize the free-free radiation spectra generated during collisions with small impact parameter $b < b_{90}$. A particle in a small angle collision is deflected by an angle of $\theta > \pi/2$. The exact treatment of such collisions is beyond the scope of this thesis and is not further considered in the analysis. Most of the energy is radiated during the close approach of the electron to the ion on frequency ω_c. It can be determined using:

$$\left.\frac{dE}{d\nu}\right|_{\omega_c} = \frac{1}{4\pi\varepsilon_0}\frac{4e^2}{3c^3}\left(\dot{v}_c\Delta t_c\right)^2 \tag{3.3}$$

where the subscript c denotes the close approach. A sketch of a small angle collision is shown in fig. 3.3. A number of approximations can be deduced. The duration of the close approach can be taken as $\Delta t_0 \approx 2r_0/v_0$ and the distance between the ion and electron during the close approach is $r \approx r_0$. The acceleration $\dot{v}$ of the electron during the close approach is obtained from the Coulomb force:

$$\dot{v} = \frac{F_c}{m_e} = \frac{1}{4\pi\varepsilon_0 m_e}\frac{Ze^2}{r_c^2} \tag{3.4}$$

Applying approximations for the close approach on eq. (3.3) and using the conservation of the angular momentum $vb = v_0 r_0$ results in the formula for energy radiated per single electron-ion collision with impact the parameter b and incident electron velocity v:

$$\left.\frac{dE}{d\nu}\right|_{\omega_c} = \frac{8Z^2e^6}{(4\pi\varepsilon_0)^3 3c^3 m_e^2 v^2 b^2} \tag{3.5}$$

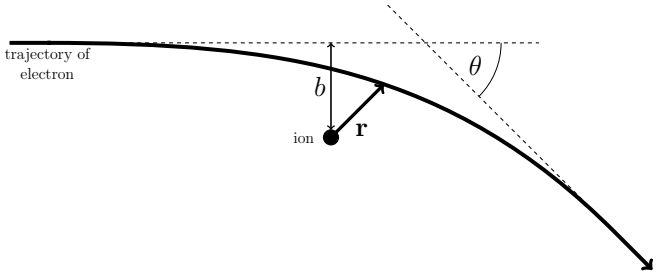

Figure 3.1: Geometry of Coulomb collision, where θ is the recoil angle, b is the impact parameter and $\mathbf{r}$ is position vector of the electron.

3.1.2 Spectrum of Free-Free Radiation from Maxwellian Plasma

In order to derive the formula for free-free radiation spectra generated in a plasma volume, averaging of the previous result eq. (3.5) over impact parameters b and incident velocities $\mathbf{v} = \mathbf{v}_i - \mathbf{v}_e$ has to be done. The averaging over impact velocities can be simplified by taking the mass ratio of electrons and ions into account. If the electron and ion temperatures are equal, the ion velocities are approximately four orders of magnitude smaller than the electron velocities. Hence, the ion velocities can be disregarded. The impact velocity reduces to $\mathbf{v} = \mathbf{v}_e$. Averaging over the ion velocity distribution yields the ion density N_i. Another simplification can be made for isotropic plasmas. If plasma is isotropic, it is sufficient to assume uniform spatial distribution of the radiation which drops the spatial dependence of $\mathbf{v}_e$. The number of collisions per unit volume with the incident velocity v and the impact parameter b is determined by $2\pi bv\mathrm{d}b$. Averaging over impact parameters the power spectral density is:

$$\begin{aligned}\frac{dP}{d\nu} =& \frac{32\pi^2 Z^2 e^6}{(4\pi\varepsilon_0)^3 3c^3 m_e^2 v} \int_{b_{min}}^{b_{max}} \frac{1}{b}\,\mathrm{d}b \\ =& \frac{32\pi^2 Z^2 e^6}{(4\pi\varepsilon_0)^3 3c^3 m_e^2 v} G(v,\nu)\end{aligned} \tag{3.6}$$

where the function $G(v,\nu)$ is a correction factor given by range of the impact parameter b. Averaging the result from eq. (3.6) over the velocity distribution results in the expression for power spectral density $S(\nu)$ (power generated per unit frequency per unit volume). The procedure is described in [12] and the final formula for the power spectral density is:

$$S(\nu) = 4\pi j(\nu) = N n_e Z^2 \left(\frac{e^2}{4\pi\varepsilon_0}\right)^3 \frac{32\pi^2}{3\sqrt{3} m_e^2 c^3} \sqrt{\frac{2m_e}{\pi eT}}\, exp\left(-\frac{h\nu}{eT}\right) \overline{g} \tag{3.7}$$

where $j(\nu)$ is the emissivity (power generated per unit solid angle, per unit volume per frequency), $\overline{g}$ is the Maxwell-averaged gaunt factor. The exponential term results from the limits of integration. The upper limit is ∞ and the lower limit has to be set to $E = h\nu$. The lower limit is determined by the maximum energy which can be radiated during a free-free interaction. The energy has to be lower than the incident kinetic energy of the electron, otherwise the electron becomes bound to the ion. The radiated power is linearly dependent on the ion and electron density and increases with the square of the ion charge. If plasma consists of multiple ionic species with different charge states, the charge number Z is replaced by the effective charge number Z_eff which takes the increase of radiation with ion charge into account. The effective charge number is given by:

$$Z_{eff} = \frac{\sum_i Z_s N_s}{\sum_s N_s} \tag{3.8}$$

where the summation is performed over all ionic species. In fig. 3.2 spectral densities were obtained by evaluating eq. (3.7) with charge number $Z = 1$ and electron densities $n_e = 5 \cdot 10^{13} cm^{-3}$. By examining fig. 3.2, the difference in the rate of decay of $S(\nu)$ with frequency ν in case of different electron temperatures is obvious. Comparing results with different Gaunt factors $\overline{g}$ shows that the shape of the spectrum is mainly governed by the exponential term in eq. (3.7).

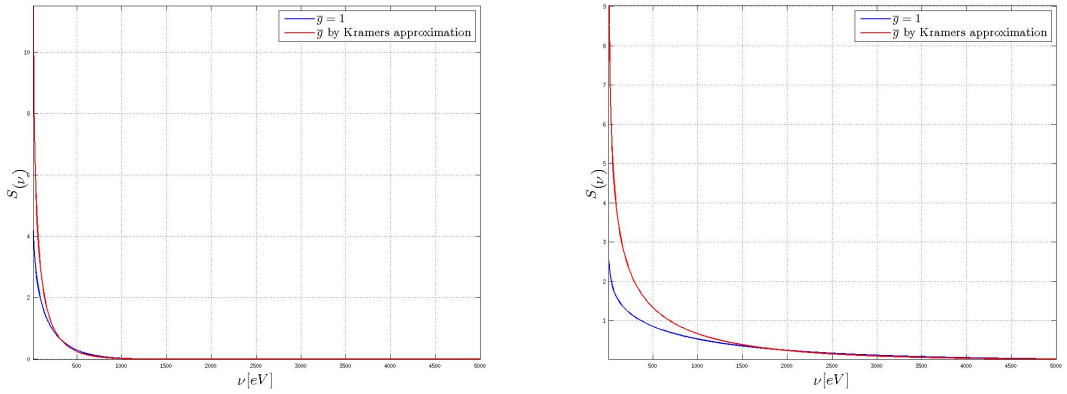

(a) Electron temperature $T_e = 500\, eV$ (b) Electron temperature $T_e = 3000\, eV$

Figure 3.2: Power spectral density $S(\nu)\,[W\, m^{-3}\, eV^{-1}]$. of free-free radiation procuded in plasma with two different electron temperatures. Valuses of $S(\nu)$ were obtained evaluating eq. (3.7) with electron densities $n_e = 5 \cdot 10^{19} m^{-3}$ and ion charge number $Z = 1$.

3.1.3 Gaunt Factor

The classical approach to the derivation of spectral characteristics of the free-free radiation and approximations taken in the process (e.g. neglecting large angle collisions) introduce errors. The errors are partly removed by applying the Maxwell-averaged Gaunt factors $\overline{g}$. Approximative solutions of $\overline{g}$ are given in [12, 14]. For Maxwellian plasma with $T_e << Z^2 R_y$ and for low frequencies, [12] gives semi classical Kramer's approximation for $\overline{g}$:

$$\overline{g}(\nu, T_e) = \frac{\sqrt{3}}{\pi} ln \left| \left(\frac{2kT_e}{\zeta m_e} \right)^{\frac{3}{2}} \frac{2m_e}{\zeta 2\pi\nu} \left(\frac{4\pi\varepsilon_0}{Ze^2} \right) \right| \tag{3.9}$$

where $\zeta = 0.577$ is Euler's constant. The Born approximation for $T_e >> Z^2 R_y$ given in [14] is:

$$\overline{g}(\nu, T_e) = \frac{\sqrt{3}}{\pi} \mathrm{K}_0 \left(\frac{h\nu}{2kT_e} \right) exp \left(\frac{h\nu}{2kT_e} \right) \tag{3.10}$$

where K_0 is a modified Bessel function of the second kind. Latter approximations of Gaunt factors are evaluated in fig. 3.3 for two different cases of charge number Z. Comparing results for $\overline{g}$ for $Z = 30$ shows that in case of ions with high charge states Kramer's approximation seems to be invalid. Values of Gaunt factors calculated by Kramer's approximation become negative for higher frequencies.

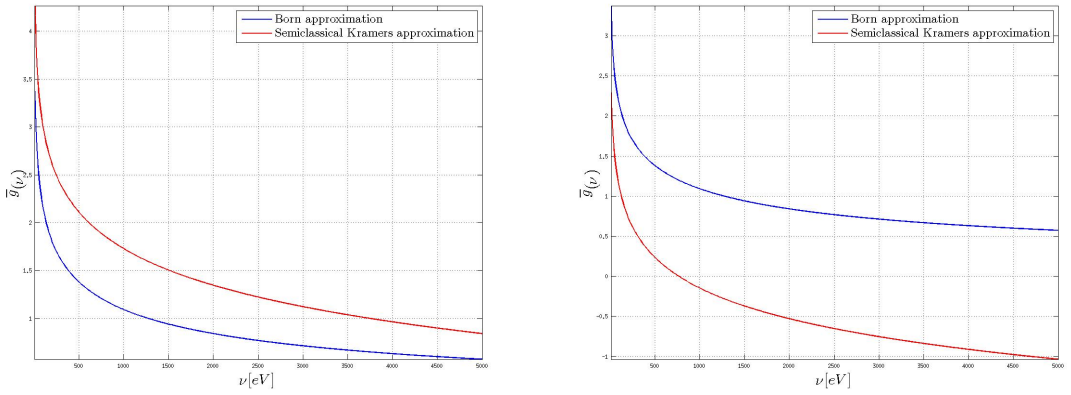

(a) Ion charge number $Z = 1$ (b) Ion charge number $Z = 30$

Figure 3.3: Maxwell averaged Gaunt factors $\overline{g}(\nu)$ obtained by low frequency semiclassical Kramers approximation and by Born approximation. The electron temperature was set to be $T_e = 2keV$.

3.2 Free-bound Radiation

Another mechanism generating x-rays is radiative recombination of free electrons with ions, also called free-bound radiation. It occurs when an electron radiates all its kinetic energy during a collision with an ion. In this case the electron occupies a vacancy in one of the empty ionic orbitals. The energy in radiative recombination is conserved by photon emission. The photon carries energy is given by the sum of the incident kinetic energy of the electron and the binding energy of the assumed orbital:

$$h\nu = \frac{1}{2}mv^2 + \frac{E_{\zeta,m}}{n^2} \tag{3.11}$$

where n is the principal quantum number of the occupied shell. The line width $\Delta\nu$ is specified in [12] as:

$$\begin{gathered} \frac{1}{2}mv^2 + \frac{E_{\zeta,m}}{\left(n+\frac{1}{2}\right)^2} \leq h\nu \leq \frac{1}{2}mv^2 + \frac{E_{\zeta,m}}{\left(n+\frac{1}{2}\right)^2} \\ \Delta\nu_n \approx \frac{2E_{\zeta,m}}{hn^3} \end{gathered} \tag{3.12}$$

The latter expression for the line width is independent of the impact parameter and thus, the power radiated during a single electron-ion collision with initial velocity v averaged over all impact parameters is:

$$P_n = \frac{dP}{d\nu}\Delta\nu_n = \frac{32\pi^2 Z^2 e^6}{(4\pi\varepsilon_0)^3 3c^3 m_e^2 v}\frac{E_{\zeta,m}}{hn^3}G_n \tag{3.13}$$

The $dP/d\nu$ term was taken from eq. (3.6) and G_n is a gaunt factor. The process of averaging previous equation over the velocity distribution can be simplified by solving eq. (3.11) for initial electron velocity:

$$v = \sqrt{\frac{2}{m}\left(h\nu - \frac{E_{\zeta,m}}{n^2}\right)} \tag{3.14}$$

substituting eq. (3.14) for the velocity in eq. (3.13), assuming Maxwellian distribution of velocities and summing over all vacancies in orbitals gives the emissivity spectrum of the recombination radiation for an ion with charge ζ:

$$4\pi j_\zeta(\nu) = n_e Z^2 \left(\frac{e^2}{4\pi\varepsilon_0}\right)^3 \frac{32\pi^2}{3\sqrt{3}m_e^2 c^3}\sqrt{\frac{2m_e}{\pi kT_e}}\,\mathrm{e}^{-\frac{h\nu}{kT_e}}\sum_m N_{\zeta,m}\left[\frac{2E_{\zeta,m}}{T_e n^3}G_n e^{\frac{E_{\zeta,m}}{n^2 T_e}}\right] \tag{3.15}$$

where $N_{\zeta,m}$ density of ions in state ζ, m. The term in brackets describes the relative energy state of the ion and radiated the frequency. The formula is valid only for

frequencies $h\nu > E\zeta, m$, otherwise the emissivity is zero. This is due to the fact that the electron does not recombine if $\frac{1}{2}mv^2 > h\nu$. At very low frequencies ν, only shells with low principal quantum numbers contribute to the radiation and the contribution decays quickly due to the n^{-3} dependency. Equation (3.15) can be further simplified, if ions are assumed to be in ground states. A separation into two cases is suggested in [**Hitchinson**]. The first case is a recombination into the ground shell with ζ vacancies and the second cases is a recombination into fully ionized upper shells. Perfect screening by electrons in lower orbitals can be assumed for completely ionized shells. The binding energy can be expressed as $\frac{Z^2 R_y}{n^2}$. Therefore, equation (3.15) can be rewritten as:

$$\begin{aligned} 4\pi j_\zeta(\nu) =& n_e Z^2 \left(\frac{e^2}{4\pi\varepsilon_0}\right)^3 \frac{32\pi^2}{3\sqrt{3}m_e^2 c^3}\sqrt{\frac{2m_e}{\pi k T_e}}\, \mathrm{e}^{-\frac{h\nu}{kT_e}} \times \\ & \left\{ N_k \frac{2\xi Z^2 R_y}{T_e k^3} G_k e^{\frac{Z^2 R_y}{k^2 T_e}} + \sum_{m,n>k} N_m \frac{2E_m}{T_e n^3} G_n e^{\frac{E_m}{n^2 T_e}} \right\}\Bigg|_{k=min(n)} \end{aligned} \tag{3.16}$$

where the first term in brackets is recombination to the lowest unfilled shell $k = min(n)$ and ξ is the number of vacancies in shell k. The second term is the recombination to higher empty shells.

3.3 Line Radiation

As previously described, one source of electromagnetic radiation is spontaneous decay of excited atomic states. This phenomenon occurs in plasma due to atomic processes which are constantly exciting ions. If the energy difference between initial and final state of the atom is high enough, a photon within the x-ray spectrum is radiated. The position of lines in the spectrum is unique for every element because of different orbital energies. The spectral power density is determined by atomic elements present in plasma and by the electron temperature. Elements with low atomic numbers are fully ionized above certain electron temperatures and do not generate any line spectra. Line emission becomes the most important mechanism of radiation for ions with high Z which are not fully ionized. In tokamaks it can be materials from which the vessel wall is made e.g. tungsten.

3.3.1 Line Spectra Power Density

The emission in a spectral line $\delta_{m'\to m}$ $[photons \cdot cm^{-3} \cdot s^{-1}]$ is determined by the rate of spontaneous decay (sect: 2.2.1) of an ion in the the state ζ, m' to the state with

lower energy ζ, m:

$$\delta_{h\nu} = N_{\zeta,m}\mathcal{A}\left(\zeta, m' \rightarrow \zeta, m\right) \tag{3.17}$$

where $\delta_{h\nu}$ is the emission in the spectral line. The frequency of the line is determined by the difference of energies of the initial ion state ζ, m' and the final state ζ, m. The Einstein coefficient $\mathcal{A}$ gives the probability of spontaneous decay and $N_{\zeta,m'}$ is the number density of the initial ion state. If the model for low plasma density presented in sect: 2.3.4 is used, the number density $N_{\zeta,m'}$ can be found using eq. (2.23). The spectral power density $P_{\zeta,m'\rightarrow m}\left(\nu\right)$ of the line can be found by multiplying eq. (3.17) with the energy of the photons:

$$P_{\zeta,m'\rightarrow m}\left(\nu\right) = N_{\zeta,m}\mathcal{A}\left(\zeta, m' \rightarrow \zeta, m\right) \int h\nu\mathcal{L}(\nu)d\nu \tag{3.18}$$

The function $\mathcal{L}(\nu)$ in eq. (3.18) is the line profile. The line profile applies effects of line broadening and is generally a function of a unit area. The spectral power density of the line spectrum is obtained by adding spectral contributions of all transitions $\zeta, m' \rightarrow m$ occurring in plasma. For plasma containing elements with low Z, the spectrum consists of clearly separated spectral lines. The number of lines in the spectrum grows with the atomic number of elements. With increasing number of lines the spacing between spectral lines decreases. At a certain point individual spectral lines start to correlate. Spectrum with these properties is called Unresolved Transition Array (UTA). An example of the complexity of the UTA is shown in [13], where the number of possible transitions between configurations $3d^3 4f^1 \rightarrow 3d^4$ is computed to be 5523. modelling of the UTA becomes an unmanageable task, if all effects of line broadening and satellites should be included. An example of computed UTA is given in fig. 3.4.

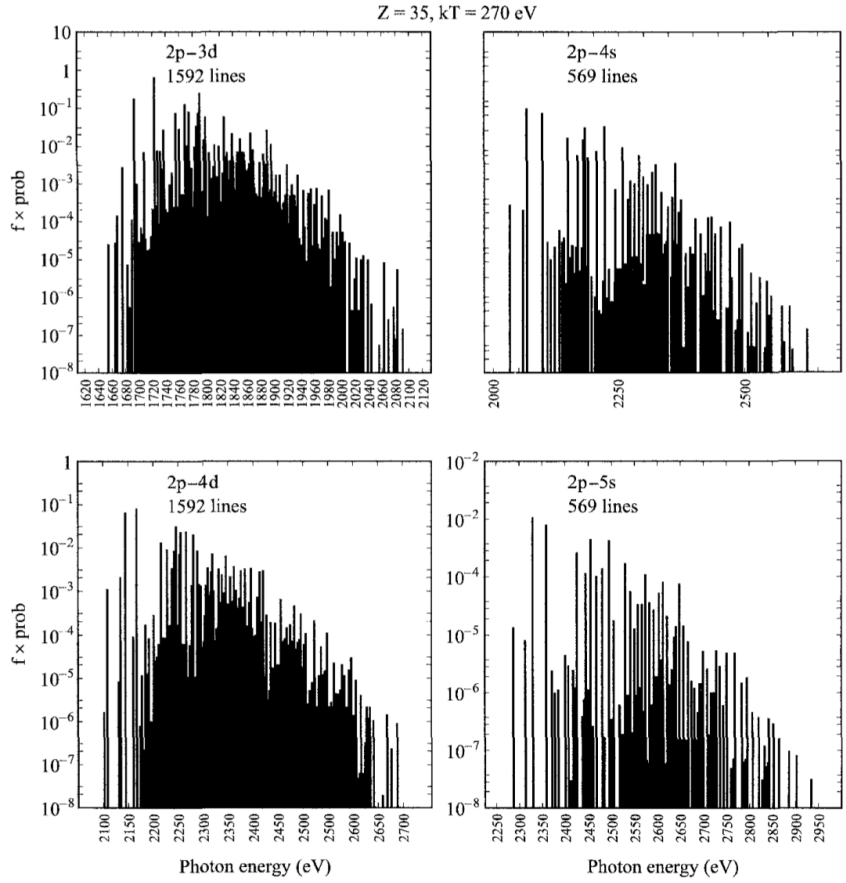

Figure 3.4: Computed emission spectrum of the $2p-3d, 2p-4s, 2p-4d, 2p-5s$ transitions for bromine plasma at T=270eV and $n_i = 2 \cdot 10^{20} cm^{-3}$. Reprinted from [13].

Chapter 4

Data Analysis

4.1 Algorithm Description

In this chapter the algorithm used for the estimation of the tungsten density and the values of correction coefficients for tomographic reconstruction is described. Data provided for this work contain profiles of electron temperature and power density of soft x-rays generated in plasma. Both quantities are provided for each of 68×40 pixels into which the cross-section of plasma is divided. Values of the power density for each pixel are results of tomographic reconstruction as measured by the horizontal camera. Cameras at JET act as filters with different spectral sensitivities. This is caused by different types of cameras and by different thicknesses of reactor walls (made of beryllium) separating the cameras from the plasma. Spectral sensitivities of vertical and horizontal cameras with included influence of the wall will be denoted $V(\nu)$ and $H(\nu)$, respectively. Further on, variables with subscript V and H will stand for quantities measured by vertical and horizontal camera, respectively. These variables contain data filtered by spectral characteristics of the cameras. If a variable containing information about radiation is not denoted by any subscript, it is as generated by plasma. Value of correction coefficients are the ratios between intensities measured by the V-camera and the H-camera in each pixel. For pixel i, j it is:

$$C|_{i,j} = \left.\frac{S_V}{S_H}\right|_{ij} = \left.\frac{S_{V,ff} + S_{V,fb} + S_{V,l}}{S_{H,ff} + S_{H,fb} + S_{H,l}}\right|_{ij} \tag{4.1}$$

where the quantity $S(\nu)$ is the power spectral density of the radiation generated by plasma. The power spectral density S can be decomposed into three contributors. The first contributor is free-free radiation which will be denoted by the subscript ff, the second is free-bound radiation which will be denoted by the subscript fb and the last contributor is line radiation which will be denoted with the subscript l. The latter can

be expressed as:

$$\begin{aligned} S_{ff} &= n_e^2 R_{ff}(T_e) \\ S_{fb} &= n_e N_T R_{fb}(T_e) \\ S_l &= n_e N_T R_l(T_e) \end{aligned} \tag{4.2}$$

where the quantity R is the radiation coefficient. It is the power generated per interacting particles and has units $[Wcm^3]$. The advantage of the radiation coefficient is its dependence on electron temperature T_e only. This allows for an estimation of the radiation coefficients without knowledge of the electron and ion densities. Rearranging eq. (4.1) gives:

$$\begin{aligned} C_{i,j} &= \left. \frac{n_e^2 R_{V,ff}(T_e) + n_e N_T R_{V,fb}(T_e) + n_e N_T R_{V,l}(T_e)}{n_e^2 R_{H,ff}(T_e) + n_e N_T R_{H,fb}(T_e) + n_e N_T R_{H,l}(T_e)} \right|_{ij} \\ &= \left. \frac{\int V(\nu) \left[n_e^2 R_{ff}(T_e, \nu) + n_e N_T R_{fb}(T_e, \nu) + n_e N_T R_l(T_e, \nu) \right] \mathrm{d}\nu}{\int H(\nu) \left[n_e^2 R_{ff}(T_e, \nu) + n_e N_T R_{fb}(T_e, \nu) + n_e N_T R_l(T_e, \nu) \right] \mathrm{d}\nu} \right|_{ij} \end{aligned} \tag{4.3}$$

In order to compute correction coefficients $C_{i,j}$, the values of the radiation coefficients $R(T_e)$ are to be found. This can be done by using their spectral properties $R(Te, \nu)$. $R_{ff}(Te, \nu)$ can be modelled by previously derived analytic formulas. Atomic data provided by OPEN-ADAS are employed to model $R_l(Te, \nu)$ and $R_{fb}(\nu)$. OPEN-ADAS is a database of publicly accessible data from ADAS (Atomic Data and Analysis Structure). The database contains rates of atomic processes which allow for modelling of various properties of plasma, e.g. the radiation spectrum and the ionization balance. Two sets of data for tungsten from OPEN-ADAS are used in this thesis project. The first set ADF11 contains effective recombination and ionization coefficients. The second set ADF15 contains photon emissivity coefficients for spectral lines. As a first step in estimating $C_{i,j}$, the ionization balance of tungsten plasma at electron temperature T_e is modelled. The output of the model is P_ζ which is the probability of tungsten ions having the charge ζ. P_ζ is used together with data from ADF15 in order to model $R_l(T_e, \nu)$ and also as an input to model $R_{fb}(\nu)$. The estimation of the electron density profile n_e in a pixel is based on data from the set T_81835_51p1s. This can be done due to the fact that the tungsten density in this experiment can be assumed zero. In order to find the tungsten density profiles in data sets T_82722_45p2s, T_82722_46p3s and T_82722_47p5s, the electron density is assumed to be the same in all experiments. The values of n_e and N_T are plugged into eq. (4.3) to find the values of correction coefficients.

4.2 Tomographic Reconstruction of Radiated Power Density

The data provided for analysis were measured during two experiments made by JET. Electron temperature values for each pixel and tomographic reconstructions the of radiated power density as seen by H-camera are included (courtesy of Assoc. Prof. Jan Mlynář). The data are displayed in fig. 4.1, fig. 4.2, fig. 4.3 and fig. 4.4. In each figure the sub-figure *a*) shows tomographic reconstruction of the radiated power density in Wcm^{-3}. Sub-figure *b*) displays values of electron temperatures T_e in $[eV]$. The distribution of S and T_e in the fig. 4.1 follows the same pattern. The radiated power density S in a pixel seems to be governed by the temperature value in the corresponding pixel only. This does not apply for the rest of the figures. Maxima of radiated power densities are not located in the centre of the plasma and do not correspond to positions of temperature maxima. This suggests that the abundance of heavy elements in the plasma in fig. 4.1 is insignificant and that plasmas in the figures fig. 4.2, fig. 4.3 and fig. 4.4 contain significant amounts of tungsten impurities.

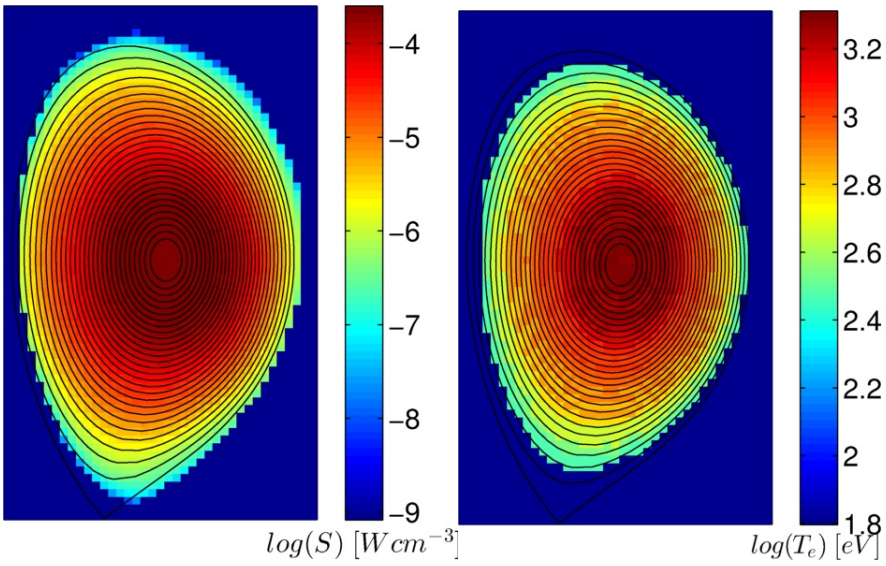

(a) Radiated power density (b) Electron emperature

Figure 4.1: Tomographic reconstruction of radiated power density as seen by H-camera and measured electron temperatures (data id: T_81835_51p1s). With courtesy of Assoc. Prof. Jan Mlynář.

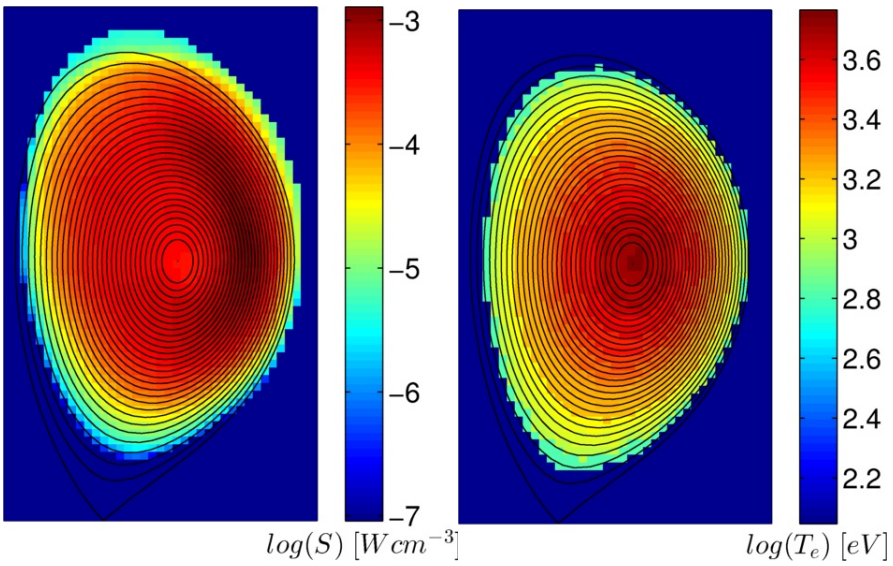

(a) Radiated power density (b) Electron emperature

Figure 4.2: Tomographic reconstruction of radiated power density as seen by H-camera and measured electron temperatures (data id: T_81835_51p1s). With courtesy of Assoc. Prof. Jan Mlynář.

4.3 Probability Distribution of Charge States of Tungsten Atoms

In order deliver the model of power spectral densities generated by plasma, the distribution of charge states of tungsten ions inside the plasma has to be found. This can be modelled by using ionization and recombination coefficients, if electron temperatures and electron densities in pixels are known. In this section a brief description of the applied ionization balance model is given. The results of probability distributions of charge states and their dependence on the electron temperature and the electron density are presented.

4.3.1 Ionization Balance

The ionization balance in plasma can be delivered by using equation for impurity transport model [16]:

$$\frac{\partial N_\zeta}{\partial t} = -\nabla \cdot \Gamma_\zeta + Sources - Sinks \tag{4.4}$$

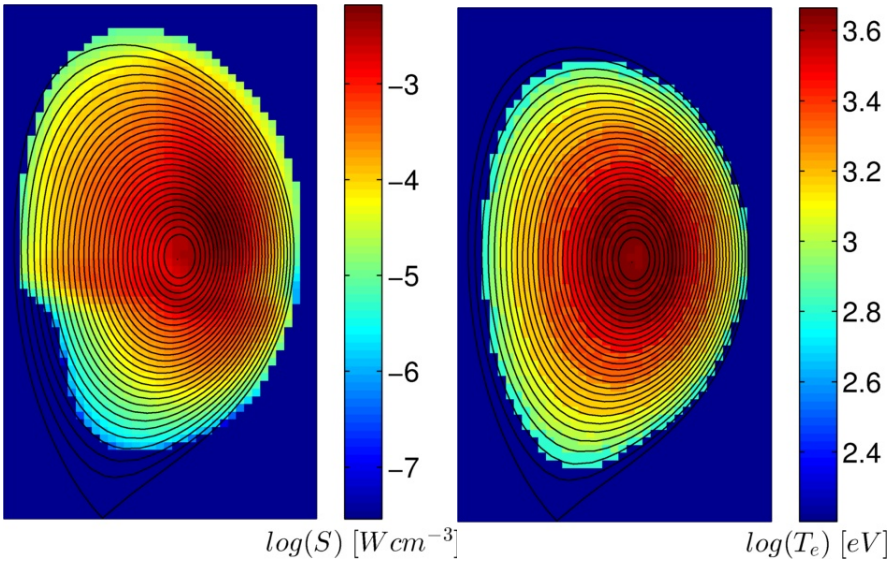

(a) Radiated power density (b) Electron emperature

Figure 4.3: Tomographic reconstruction of radiated power density as seen by H-camera and measured electron temperatures (data id: T_81835_51p1s). With courtesy of Assoc. Prof. Jan Mlynář.

where the N_ζ is the density of ions with the charge ζ and Γ_ζ is the flux of ions from the pixel. The particle transport between pixels will be neglected for simplicity reasons. This can be justified by short life time of metastable states of tungsten $\approx 10/Z^8\ s$[16]. Disregarding the transport of impurities allows for building model of ionization balance with knowledge of electron and ion densities only. This simplification is crucial because no data for particle transport were available. With Γ_ζ neglected the eq. (4.4) can be then rewritten as:

$$\frac{\partial N_\zeta}{\partial t} = Sources - Sinks \tag{4.5}$$

Sources and Sinks stand for all atomic processes populating and depopulating the charge state ζ, as described in sect: 2.3.1. Assuming that the plasma in a pixel is in coronal equilibrium, only the density of ground state ions is assumed to be significant and densities of metastable states and shortly lived excited states are assumed to be zero. The state ζ is depopulated by ionization and recombination and populated by ionization from the state below and recombination from the state above only. The corona equilibrium model also implies steady state conditions in which densities of ground states are constant. Applying this to the eq. (4.5), it can be then rewritten as follows:

$$\left[\mathcal{R}_\zeta\left(T_e, n_e\right) + \mathcal{I}_\zeta\left(T_e, n_e\right)\right] N_\zeta = \mathcal{I}\left(T_e, n_e\right)_{\zeta-1} N_{z-1} + \mathcal{R}_{\zeta+1}\left(T_e, n_e\right) N_{\zeta+1} \tag{4.6}$$

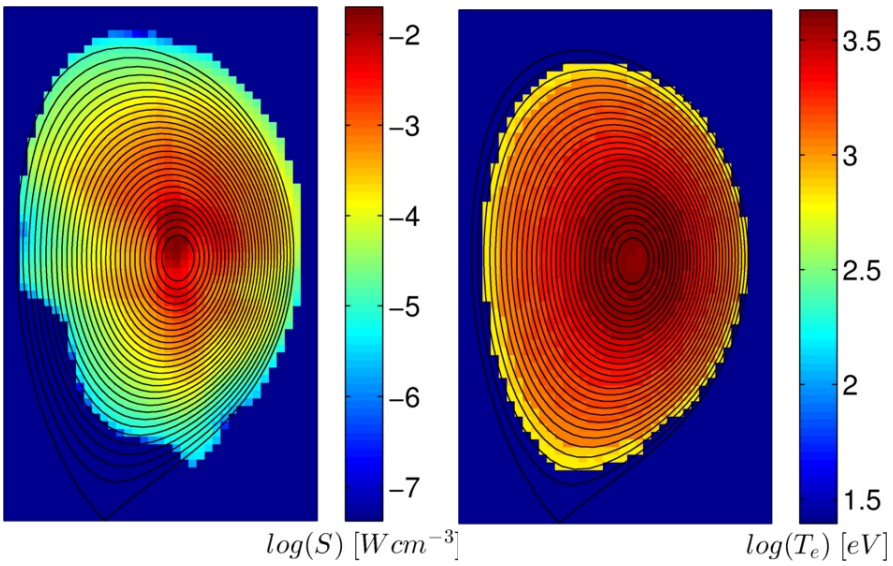

(a) Radiated power density (b) Electron emperature

Figure 4.4: Tomographic reconstruction of radiated power density as seen by H-camera and measured electron temperatures (data id: T_81835_51p1s). With courtesy of Assoc. Prof. Jan Mlynář.

where $\mathcal{I}_x$ and $\mathcal{R}_x$ are the ionization and the recombination coefficients of state x, respectively. Both coefficients are functions of electron temperatures and densities (for the reasons of better overview the notation for the dependencies will be omitted). A set of equations from eq. (4.6) can be constructed and solved for the densities of individual charge states of tungsten atoms. Writing it in matrix form results in:

$$\mathbf{C} \cdot \mathbf{N} = 0 \tag{4.7}$$

where

$$\mathbf{C} = \begin{pmatrix} -\mathcal{I}_0 & \mathcal{R}_1 & 0 & 0 & 0 & \cdots & 0 & 0 & 0 \\ \mathcal{I}_0 & -(\mathcal{I}_1+\mathcal{R}_1) & \mathcal{R}_2 & 0 & 0 & \cdots & 0 & 0 & 0 \\ 0 & \mathcal{I}_1 & -(\mathcal{I}_2+\mathcal{R}_2) & \mathcal{R}_3 & 0 & \cdots & 0 & 0 & 0 \\ & & & & & \ddots & & & \\ 0 & 0 & 0 & 0 & 0 & \cdots & \mathcal{I}_{M-2} & -(\mathcal{I}_{M-1}+\mathcal{R}_{M-1}) & \mathcal{R}_M \\ 0 & 0 & 0 & 0 & 0 & \cdots & 0 & \mathcal{I}_{M-1} & -\mathcal{R}_M \end{pmatrix}$$

$$\mathbf{N} = \begin{pmatrix} P_0 \\ P_1 \\ \vdots \\ P_M \end{pmatrix} \tag{4.8}$$

The densities of atomic charges N_ζ were replaced by probabilities, for which the following condition applies:

$$P_\zeta = \frac{N_\zeta}{\sum_\zeta N_\zeta} \tag{4.9}$$

4.3.2 Modelling of Probability Distribution of Charge States of Tungsten Atoms

Ionization and recombination coefficients for tungsten were obtained from OPEN-ADAS [17]. Namely from files *acd*50_*w.dat* and *scd*50_*w.dat*. The files contain ionization and recombination coefficients for all ionization levels of tungsten and for a range of electron temperatures and electron densities. Once the data were loaded, the coefficients for specific input values of T_e and n_e were obtained by linear interpolation. Interpolated coefficients were subsequently used to solve eq. (4.7) for the probabilities P_ζ. The obtained results of P_ζ and the effective charge Z_{eff} are displayed in fig. 4.5 and fig. 4.6. Figure (4.5) shows the evolution of P_ζ and Z_{eff} with temperature within the range of 1000–4000eV. In fig. 4.5a only charge states with the maximum of $P_\zeta > 0.05$ in the plotted range are displayed. All charge states follow Gaussian-like curves and each of them is the most probable state for at least one electron temperature. The dependence of effective charge state of tungsten Z_{eff} for the same range of temperatures is plotted in fig. 4.5b. Two factors suggest correctness of the model:

- The growing importance of higher charge states and the increase in Z_{eff} with raising electron temperature.

- The sum over all probabilities P_ζ in fig. 4.5a gives a number very close to unity for every T_e (which was verified numerically).

The dependence of P_ζ and Z_{eff} on the electron density can be seen in fig. 4.6. The effective charge is proportional to electron density due to the increasing importance of collisional processes. Comparing dependencies of P_ζ and Z_{eff} on T_e and N_e shows that the density dependence of the plotted variables is weaker than their temperature dependence. The differences in P_ζ is in a range of 0.05 and the difference in Z_{eff} is ≈ 1 over two orders of magnitude difference in electron density. This behavior is important for a later stage of modelling, where a constant value of electron density is used to obtain ionization balance and values of rates of atomic processes.

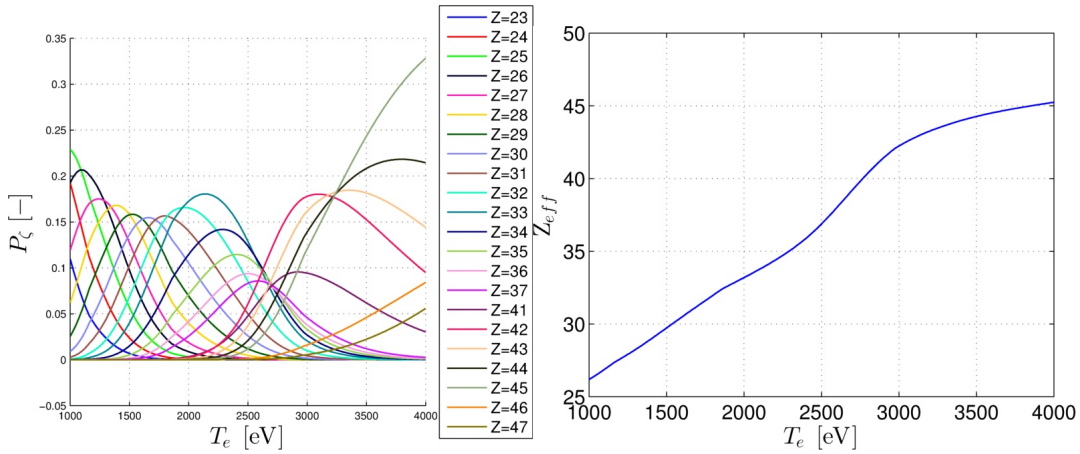

(a) Dependence of P_ζ on T_e (b) Dependence of Z_{eff} on T_e

Figure 4.5: The dependence of P_ζ and Z_{eff} on electron temperature T_e. The electron temperature was set constant $n_e = 10^{13}\text{cm}^{-3}$.

4.4 Modelling of Soft X-Ray Spectra generated by Hot Plasmas

In order estimate the density profile of tungsten in plasma and the values of correction coefficients for tomographic reconstructions, a model providing the spectra generated in a pixel has to be created. The main contributors are free-free, free-bound and line radiation. In this section models for each kind of spectra are described.

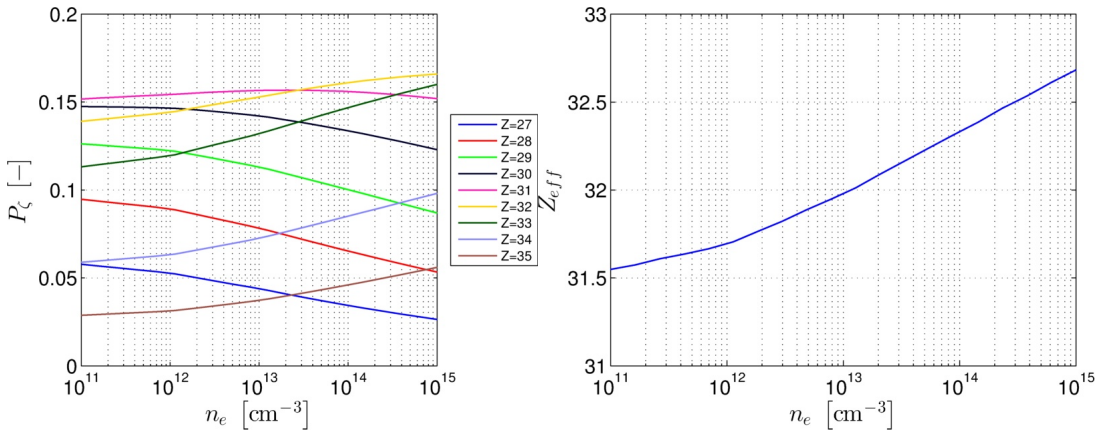

(a) Dependence of P_ζ on n_e

(b) Dependence of Z_{eff} on n_e

Figure 4.6: The dependence of P_ζ and Z_{eff} on electron density n_e. The electron temperature was set constant $T_e = 1800$eV.

4.4.1 Free-Free Radiation Spectrum generated by Hydrogen Plasma

The distribution of particle velocities in the plasma is assumed to follow the Maxwell-Boltzmann distribution. The the free-free radiation was modelled by using eq. (3.7). Three models of free-free radiation spectrum and corresponding values of Gaunt factors for three electron temperatures $T_e = 1000, 2500, 4000$eV are plotted in fig. 4.7. The plotted energy range is 10eV–30keV. Data are displayed in the form of radiation coefficients $R(\nu)$. The differences between the spectra before and after the application of gaunt corrections are relatively small, i.e. approximately in the order of 10 for the highest frequencies. The governing factor of the shape of the spectra is the electron temperature. This is also suggested by the exponential decay of radiation coefficients with photon energy, which is kept even after the corrections. In the fig. 4.8 the dependence of the free-free radiation coefficient R_{ff} on electron temperature is displayed. The power radiated by free-free radiation is proportional to the electron temperature in the plasma. Since the average kinetic energy of particles grows with the increasing temperature, this was to be expected.

4.4.2 Free-Bound Radiation Spectrum generated by Tungsten Plasma

In the model ot the free-bound radiation generated by tungsten plasma eq. (4.10) was used. Several assumptions were made before modelling. The first assumption is that

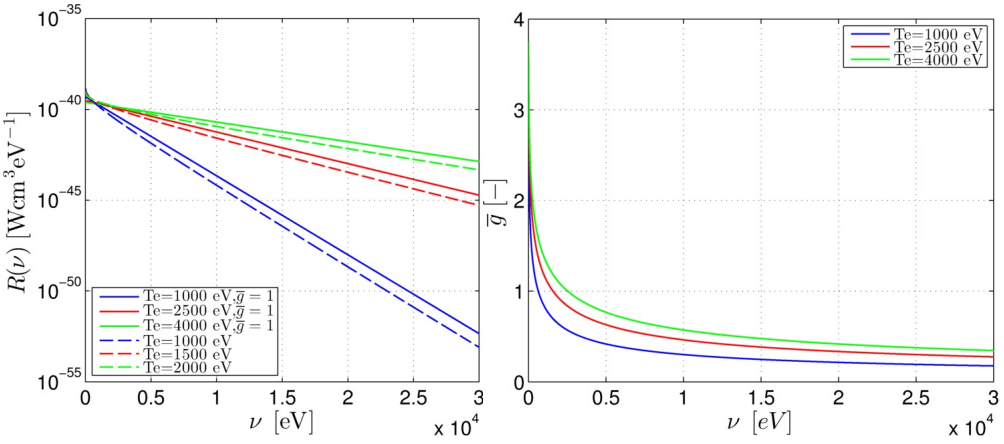

(a) Free-free radiation spectrum. (b) Values of Gaunt factors

Figure 4.7: Models of three spectra of free-free radiation generated in plasma per ion per electron and corresponding Gaunt factors. The plasma is assumed to be pure hydrogen ($Z_{eff} = 1$). Solid lines show the spectrum before corrections by Gaunt factors are applied. Dashed lines show spectrum after corrections by Gaunt factors.

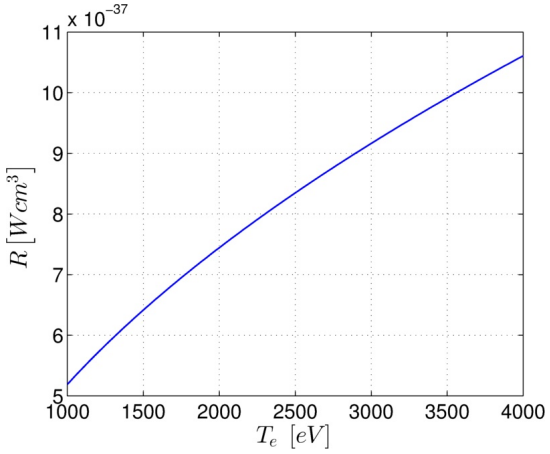

Figure 4.8: Dependence of power free-free radiation coefficient R_{ff} on electron temperature T_e.

the velocity distribution of electrons in the plasma follows the Maxwell-Boltzmann distribution. The second assumption is the electrons recombine only to the ground states which cancels out the second term in the bracket in eq. (4.10). Rewriting it here for convenience:

$$\frac{S(\nu)}{N_T n_e} = Z^2 \left(\frac{e^2}{4\pi\varepsilon_0}\right)^3 \frac{32\pi^2}{3\sqrt{3}m_e^2 c^3}\sqrt{\frac{2m_e}{\pi k T_e}}\, \mathrm{e}^{-\frac{h\nu}{kT_e}} \sum_{\zeta}\left\{P_{\zeta,k}\frac{2\xi E_\zeta}{T_e k^3} G_k e^{\frac{E_\zeta}{k^2 T_e}}\right\}\Bigg|_{k=min(n)} \tag{4.10}$$

The values of $P_{\zeta,k}$ were obtained by using the algorithm described in sect: 4.3. The ionization energies E_ζ were taken from [18] and the value of the Gaunt factor was set to be $G_k = 1$. Three free-bound spectra are plotted in eq. (4.9) . The free-bound power spectrum is a sum off contributions of all ionization states of tungsten present in plasma. The contribution of individual ion charge states can be clearly seen in fig. 4.9b as rapid increases of radiated power. Each charge state begins to contribute to the spectrum at a certain radiated energy. The contribution decays exponentially with increasing frequency of the radiated photon. The change in spectra with plasma temperature is caused by changes in distribution of ionization levels of tungsten and by increased average kinetic energies of electrons.This increase shifts the contribution of state ζ to higher radiated energies. This is caused by the fact that electrons have to radiate more energy in average to recombine with an ion during a collision. The radiation is concentrated to the part of the spectra with lower energies which can be seen in fig. 4.9b. The temperature dependence of the radiation coefficient R_{fb} is displayed in fig. 4.10. R_{fb} increases with temperature. This tendency is governed by the increasing contribution of ions with higher charges and by the higher average energy radiated per recombination event.

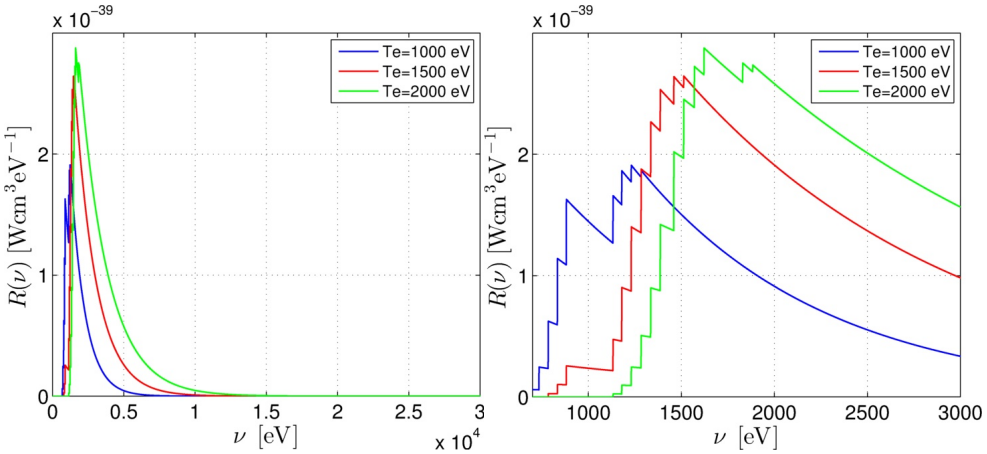

(a) Energy range $\nu = 0$–30keV. (b) Energy range $\nu = 0$–3keV.

Figure 4.9: Models of free-bound power spectral density generated by a tungsten plasma per electron per tungsten ion. Spectrum is plotted for three temperatures $T_e = 1000, 1500, 2000$eV.

4.4.3 Line Spectrum produced by Tungsten Plasma

The line spectrum produced by the presence of tungsten in plasma was modelled by using Photon Emissivity Coefficients (PEC) provided by OPEN-ADAS [17] ADF15

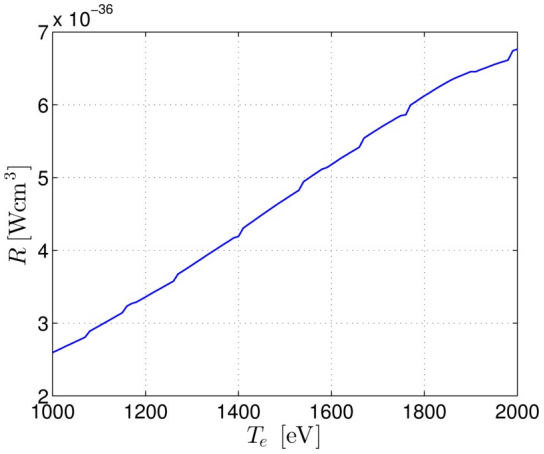

Figure 4.10: The temperature dependence of the radiation coefficient R_{fb}.

data set for tungsten. The emission in a spectral line is given by a spontaneous decay of an excited state into which it can be excited by electron impact excitation, radiative recombination or charge exchange processes. In this thesis, the emission in a spectral line was calculated with PEC of states excited by electron impact excitation only (data for other processes were not available). The emission in a spectral line $\varepsilon_{i\to j}$ normalized per ion is given by:

$$\frac{\varepsilon_{i\to j}}{N_T n_e} = \sum_{\sigma} PEC^{(exc)}_{\sigma,i\to j} P_\zeta \tag{4.11}$$

where the principles previously described in sect: 4.3 were applied to obtain P_ζ. The photon emission coefficients $PEC^{(exc)}_{\sigma,i\to j}$ were provided by OPEN-ADAS [17]. The models of three line spectra produced by tungsten plasma for electron temperatures $T_e = 1000, 25000, 4000$eV are plotted in fig. 4.11. The temperature dependence of radiation coefficient R for the line spectrum is shown in fig. 4.12. The changes in the spectral lines with the electron temperature are caused by the dependence of PEC on the temperature and by variations in P_ζ. R_l is proportional to the temperature. This is caused by increasing abundance of tungsten ions with higher charges, which generally radiate photons with higher energies.

4.5 Influence of Spectral Sensitivities of Soft X-ray Cameras on Measured Intensities

The spectral sensitivity of a camera is given by the thickness of the wall separating it from the plasma and by the camera type. Because of differences in wall thicknesses

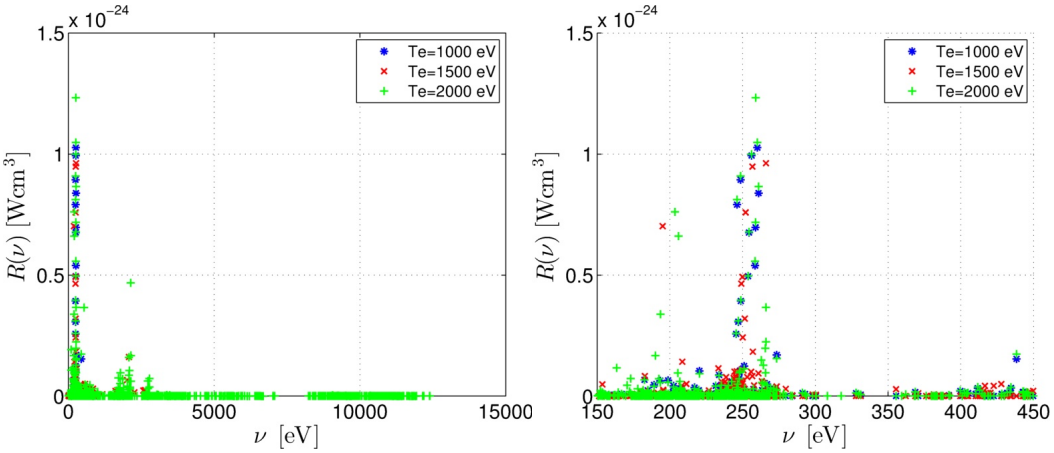

(a) Energy range $\nu = 0$–15keV (b) Energy range $\nu = 150$–350eV

Figure 4.11: Models of line spectral density generated by a tungsten plasma per electron per tungsten ion. Spectrum is plotted for three temperatures $T_e = 1000, 2500, 4000$eV.The electron density was set to $n_e = 10^{13} cm^{-3}$.

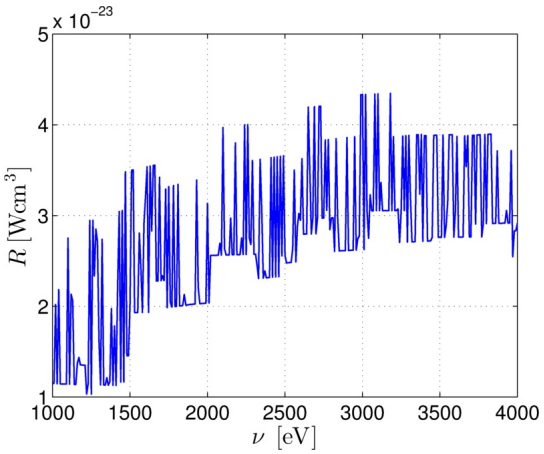

Figure 4.12: The temperature Dependence of radiation coefficient R of line radiation produced per unit volume per electron per ion.

and camera types, the spectral sensitivities of the cameras are not equal. This causes errors in tomographic reconstructions as the intensity measured by cameras differs. The spectral characteristics of V and H cameras and the difference are plotted in fig. 4.13. The spectral sensitivities of soft x-ray cameras vary the strongest in the photon energy range 1500–10000eV. Radiation in this range will cause high errors in tomographic reconstruction. Examples of models of free-free, free-bound and line radiation spectra filtered by V-camera and H-camera are displayed in fig. 4.14, fig. 4.15,

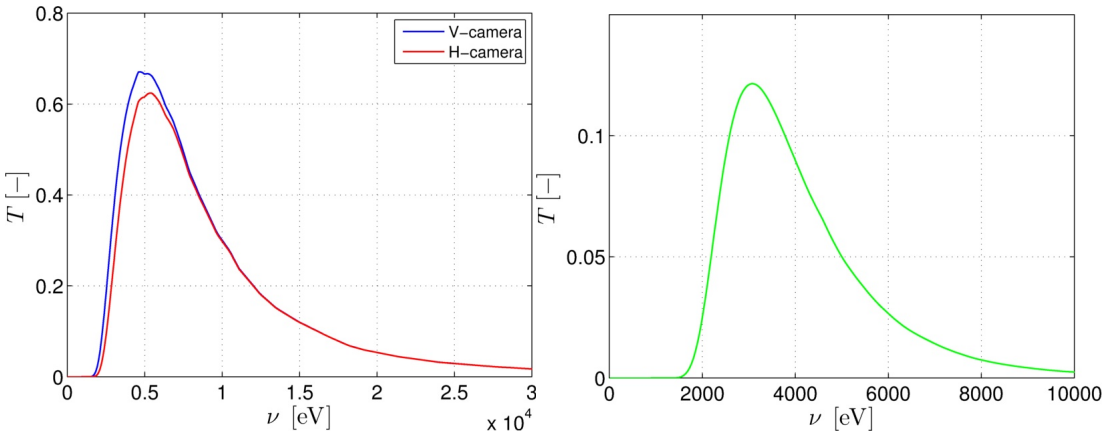

(a) Spectral sensitivities of cameras (b) Difference of spectral sensitivities of cameras

Figure 4.13: Spectral sensitivities of V and H soft x-ray cameras and the difference. Data kindly provided by Dr. Martin O'Mullane.

fig. 4.16, respectively. From the plots of the radiation coefficients R for the vertical and tge horizontal cameras it is obvious that the difference in the intensity measured by each camera depends on the electron temperature. This dependence introduces the need of modelling spectral properties of all three types of radiation for each pixel in the tomographic reconstruction. The results allow for an estimation of the tungsten ion density in the pixel and for an evaluation of the correction coefficients for tomographic reconstructions.

4.6 Estimation of Electron Density

The correction coefficients and the density of tungsten ions can be found, if the electron density profile is know. The profile was not available for any of the sets of data. It had to be calculated from T_81835_51p1s plotted in fig. 4.1. As commented on in sect: 4.2, the presence of impurities in T_81835_51p1s is considered to be negligible. This allows for neglecting the contributions of the line and the free-bound radiation in this specific data set. The electron density in a pixel i, j can be estimated from the radiated power density in the pixel and calculated radiation coefficient $R_{H,ff}$. The resulting electron density profile could subsequently be used for calculations with the other three sets of data. The formula giving the electron density value is:

$$n_e|_{i,j} = \sqrt{\left.\frac{S_H}{R_{H,ff}}\right|_{i,j}} \tag{4.12}$$

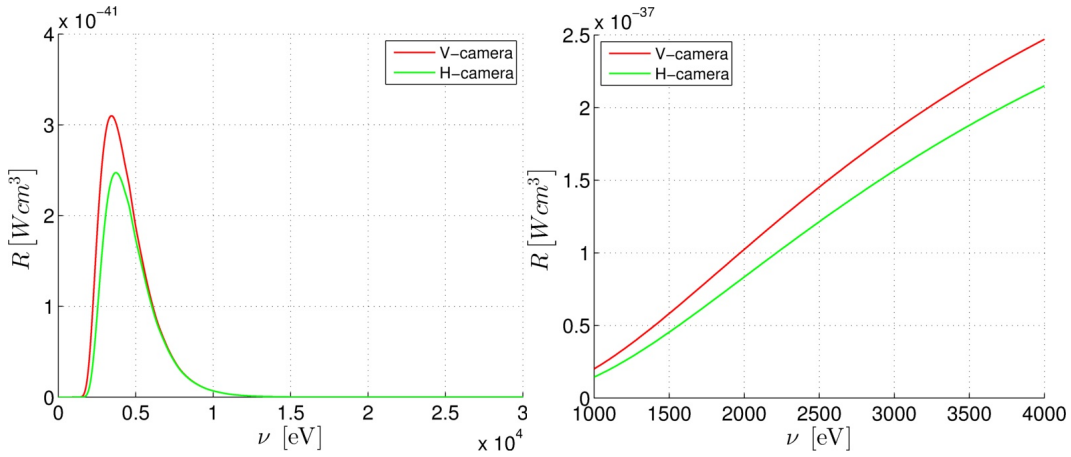

(a) Free-free radiation spectrum (b) R_{ff}

Figure 4.14: Models of free-free radiation spectra produced by hydrogen plasma at electron temperature T_e = 2.5keV filtered by vertical and horizontal cameras in (a). Sub-figure (b) shows the dependence of radiation coefficients $R_{H,l}$,$R_{V,l}$ of line radiation for vertical and horizontal cameras, respectively.

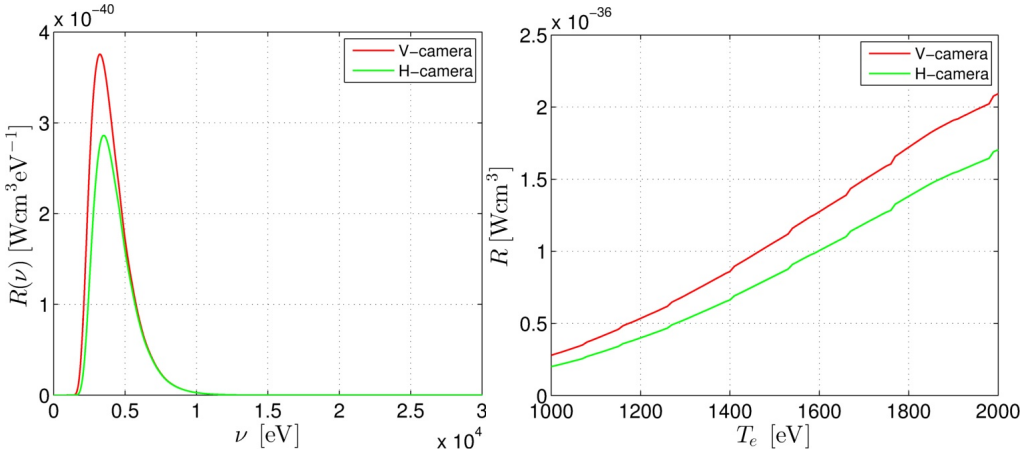

(a) Free-bound radiation spectrum (b) R_{fb}

Figure 4.15: Models of free-bound radiation spectra produced by tungsten plasma at electron temperature T_e = 2.5keV filtered by vertical and horizontal cameras in (a). Sub-figure (b) shows the dependence of radiation coefficients $R_{H,l}$,$R_{V,l}$ of line radiation for vertical and horizontal cameras, respectively.

where S_H is the radiation power density in a pixel seen by H-camera (provided by tomographic reconstruction). The $R_{V,ff}$ is the radiation coefficient of free-free radiation

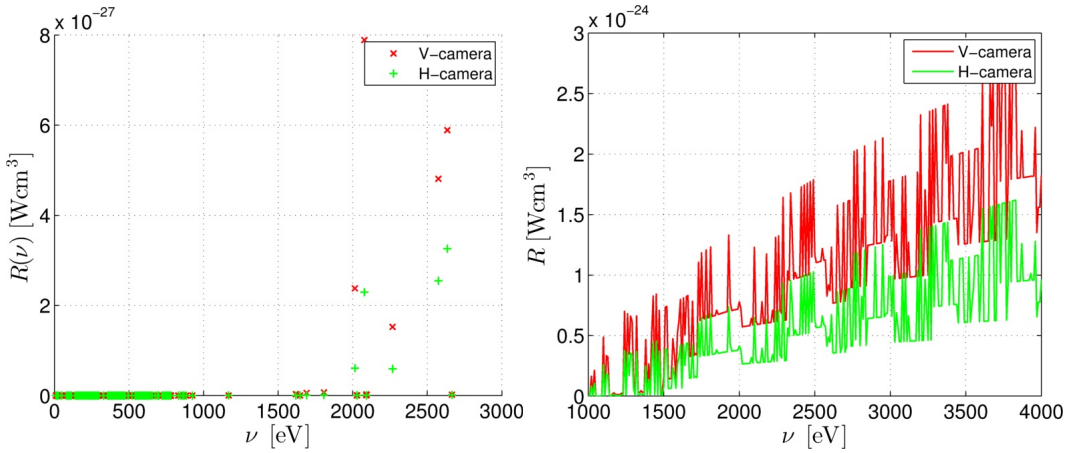

(a) Line spectrum (b) R_l

Figure 4.16: Models of line radiation spectra produced by tungsten plasma at electron temperature $T_e = 2.5$keV filtered by vertical and horizontal cameras in (a). Sub-figure (b) shows the dependence of radiation coefficients $R_{H,l}$,$R_{V,l}$ of line radiation for vertical and horizontal cameras, respectively.

filtered by the H-camera. The results are plotted in fig. 4.17. High densities at the edge of the plasma correlate with low values of radiation power density $S < 2 \cdot 10^{-6} W cm^{-3}$ and electron temperatures $T_e < 100$eV in pixels. High values at the edge may be caused by errors in the results of the tomographic reconstruction. Electron densities in the centre of the plasma are of the order of $10^{14} cm^{-3}$. Such are common for JET which suggests that assumptions made about plasma purity are justifiable. The average electron density in the the plasma is $n_e = 8.9 \cdot 10^{13} cm^{-3}$ if pixels with questionable accuracy of data are ignored.

4.7 Estimations of Contributions of Different Spectra to Radiated Power Density

The previously estimated profile of the electron density was used to calculate contributions of all three kinds of radiation to the power density generated in pixels.

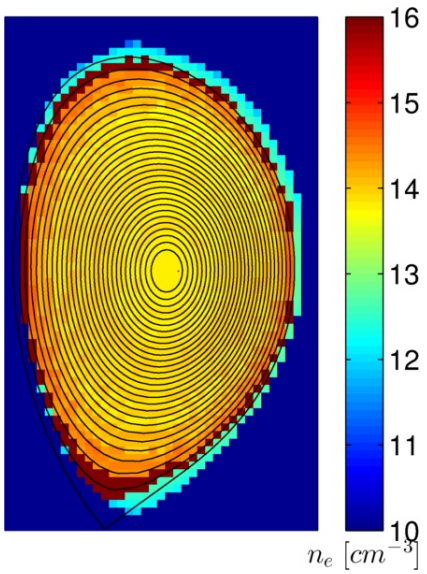

Figure 4.17: Estimation of electron density profile based on the radiation power density and electron temperature from T_81835_51p1s.

4.7.1 Estimation of Free-free radiation Contribution to Radiated Power Density

The contribution of free-free radiation to the power density radiated from a pixel is based on the value of the radiation coefficient $R_{H,ff}$ computed for the electron temperature in the pixel. The value of $S_{H,ff}$ for a pixel i, j was obtained by the evaluation of:

$$S_{V,ff}|_{i,j} = n_e^2 R_{V,ff}(T_e)\big|_{i,j} \tag{4.13}$$

The first set of results for data containing tungsten was obtained using electron density profile from fig. 4.17 and the second set of results was evaluated using the average value of electron density $n_e = 8.9 \cdot 10^{13} cm^{-3}$. The results are plotted in fig. 4.18, fig. 4.19, fig. 4.20. Sub-figures (a) contain the radiation power density based on the electron density profile from fig. 4.17 and sub-figures (b) show the results based on the constant value of electron density. Sub-figures (c) display the difference in the results of $S_{H,ff}$ between the two methods, normed to values from (b). They are on average of the order of magnitude of the radiation. Taking into account that the radiation is proportional to the square of the electron density, this can be considered an acceptable error. The advantage of results based on constant n_e is the spatial dependence given only by the electron temperature which results in symmetrical distribution of free-free radiation in plasma around the plasma centre. Results based on the electron density profile introduce additional dependence on n_e which makes the results appear noisy.

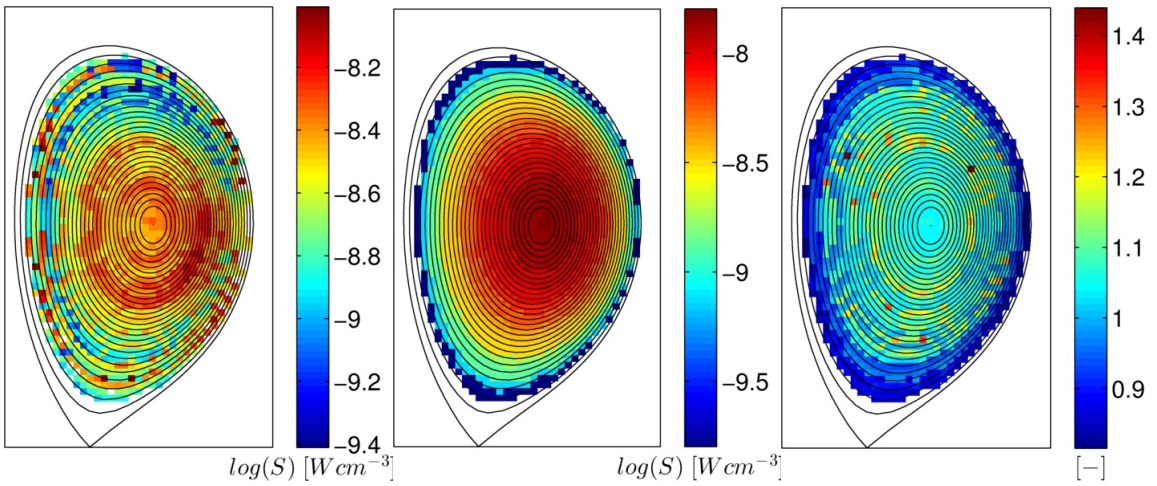

(a) $n_e(i,j)$ (b) $n_e = 8.9 \cdot 10^{13} cm^{-3}$ (c) $diff$

Figure 4.18: Modelled radiated power density contribution of free-free radiation for the data set T_82722_45p2s. Results in (a) are evaluated by using the density profile from fig. 4.17. Results in (b) are based on the constant electron density $n_e = 8.9 \cdot 10^{13} cm^{-3}$. The figure (c) displays the difference between results, normed to (b).

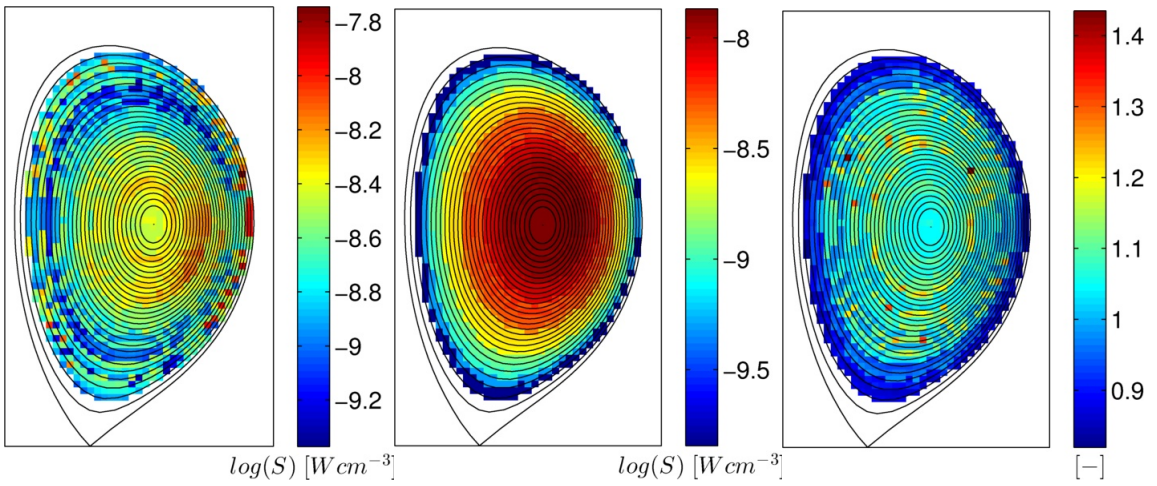

(a) $n_e(i,j)$ (b) $n_e = 8.9 \cdot 10^{13} cm^{-3}$ (c) $diff$

Figure 4.19: Modelled radiated power density contribution of the free-free radiation for the data set T_82722_45p2s. Results in (a) are evaluated using density profile from fig. 4.17. Results in (b) are based on constant electron density $n_e = 8.9 \cdot 10^{13} cm^{-3}$. The figure (c) displays the difference between results, normed to (b).

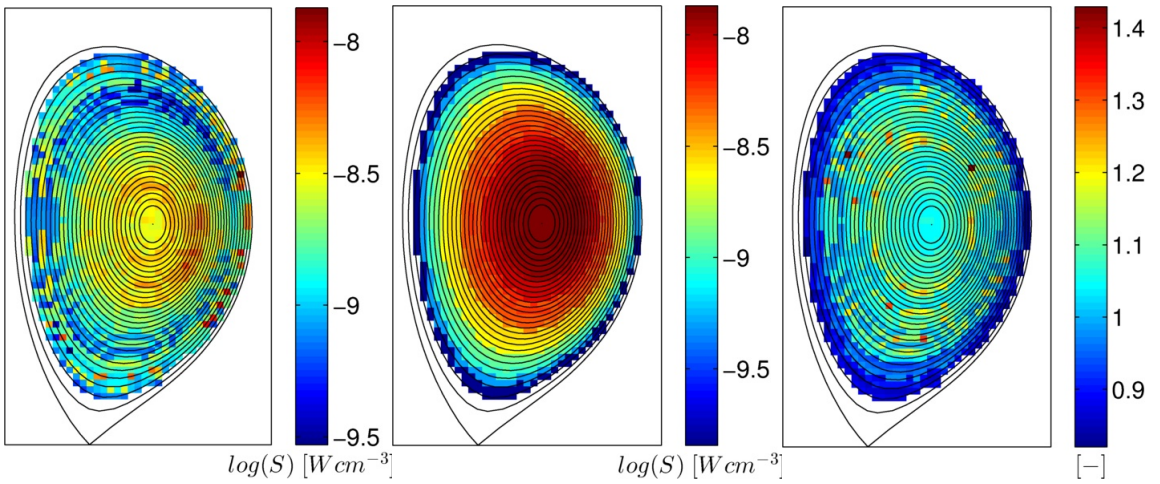

(a) $n_e(i,j)$ (b) $n_e = 8.9 \cdot 10^{13} cm^{-3}$ (c) $diff$

Figure 4.20: Modelled radiated power density contribution of free-free radiation for the data set T_82722_45p2s. Results in (a) are evaluated using density profile from fig. 4.17. Results in (b) are based on constant electron density $n_e = 8.9 \cdot 10^{13} cm^{-3}$. The figure (c) displays the difference between results, normed to (b).

4.7.2 Estimation of Line Radiation Contribution to Radiated Power Density

The contribution of the line radiation to the power density was estimated by subtracting the free-free contribution $S_{H,ff}$ as seen by the H-camera from the total power density S_H. The value of $S_{H,l}$ for a pixel i,j was obtained by evaluation of:

$$S_{H,l}|_{i,j} = (S_H - S_{H,ff})|_{i,j} \tag{4.14}$$

and the results for each data set are displayed in fig. 4.27, fig. 4.28, fig. 4.29. Sub-figures (a) are based on the electron density profile estimated in fig. 4.17. Sub-figures (b) displays $S_{H,l}$ based on the constant electron density $n_e = 8.9 \cdot 10^{13} cm^{-3}$. Sub-figures (c) show differences between both methods, normed to (b). Comparing $S_{H,l}$ with $S_{H,ff}$ allows to draw number of conclusions. The contribution of the line radiation is not negligible in each data set. This suggests the presence of tungsten ions in the plasma. The next conclusion to be made is based on the difference between both methods used. If errors at the side of the plasma are neglected, the average difference is of the order of 10^{-5} and lower. This is caused by the ratio of contributions of $S_{H,l}$ and $S_{H,ff}$ to the total radiation power density. It seems that the method of obtaining $S_{H,l}$ plays no significant role.

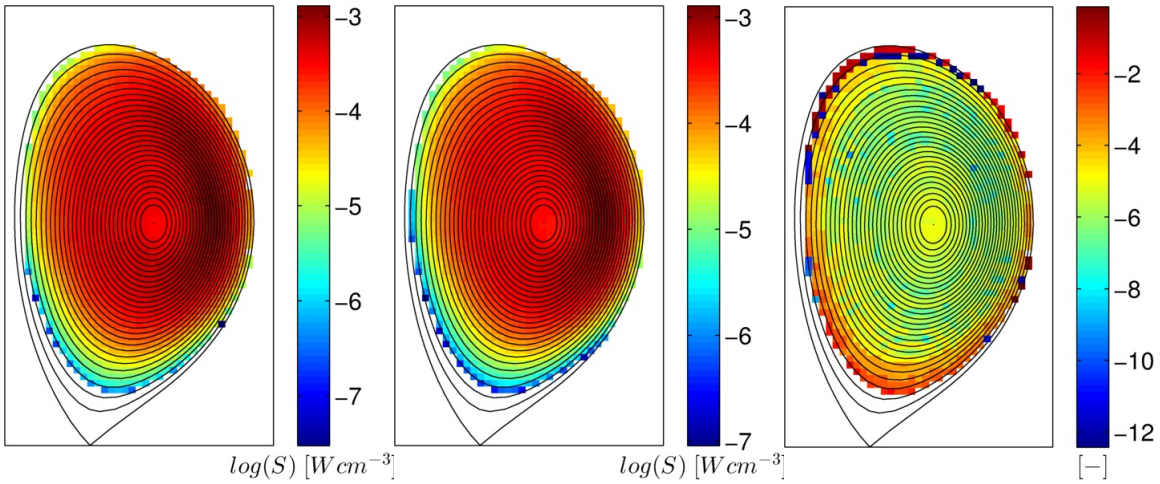

(a) $n_e(i,j)$ (b) $n_e = 8.9 \cdot 10^{13} cm^{-3}$ (c) $diff$

Figure 4.21: Estimated contribution of line radiation for the data set T_82722_45p2s. Results in (a) are evaluated by using $S_{H,ff}$ from fig. 4.18a. Results in (b) are computed using $S_{H,ff}$ from fig. 4.18b. The figure (c) displays the difference between results in (a) and (b) , normed to (b).

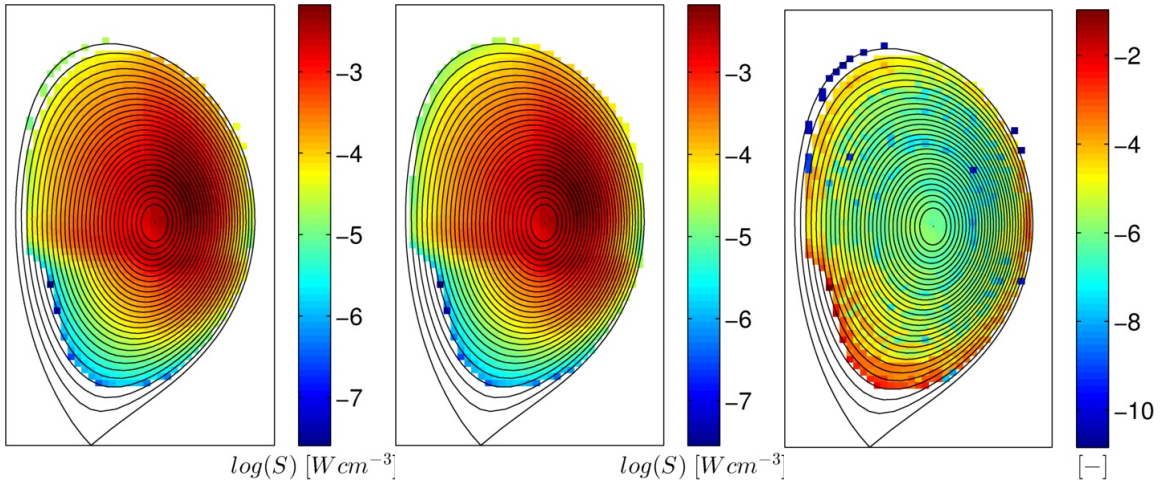

(a) $n_e(i,j)$ (b) $n_e = 8.9 \cdot 10^{13} cm^{-3}$ (c) $diff$

Figure 4.22: Estimated contribution of line radiation for the data set T_82722_46p3s. Results in (a) are evaluated using $S_{H,ff}$ from fig. 4.19a. Results in (b) are computed using $S_{H,ff}$ from fig. 4.19b. The figure (c) displays the difference between results in (a) and (b) , normed to (b).

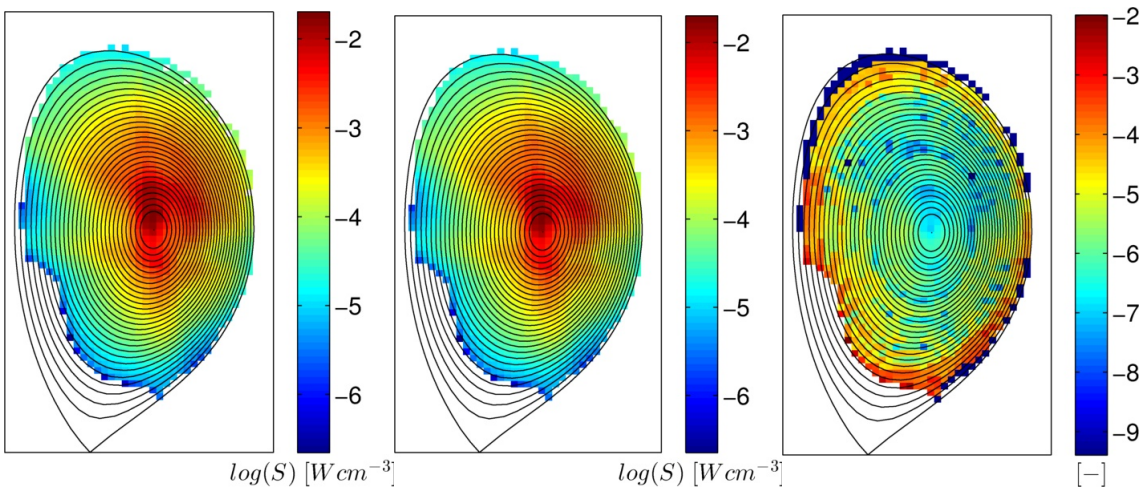

(a) $n_e(i,j)$ (b) $n_e = 8.9 \cdot 10^{13} cm^{-3}$ (c) $diff$

Figure 4.23: Estimated contribution of line radiation for the data set T_82722_47p5s. Results in (a) are evaluated using $S_{H,ff}$ from fig. 4.20a. Results in (b) are computed using $S_{H,ff}$ from fig. 4.20b. The figure (c) displays the difference between results in (a) and (b) , normed to (b).

4.8 Estimation of Density profile of Tungsten Ions

The density of tungsten ions in plasma was computed by using estimates of the electron density n_e, power density radiated by line radiation $S_{H,l}$ and the radiation coefficient for line radiation $R_{H,l}$. The density of tungsten in a pixel i,j was obtained by evaluation of:

$$N_T|_{i,j} = \left. \frac{S_{H,l}}{n_e R_{H,l}(T_e)} \right|_{i,j} \tag{4.15}$$

Both data sets were calculated by applying the electron density profile from fig. 4.17 and by taking the constant n_e into account. The results can be seen in fig. 4.29, fig. 4.29, fig. 4.29. Sub-figures (a) display data computed with the use of the results based on the electron density profile in fig. 4.17. The difference between the results obtained with both methods are negligible.

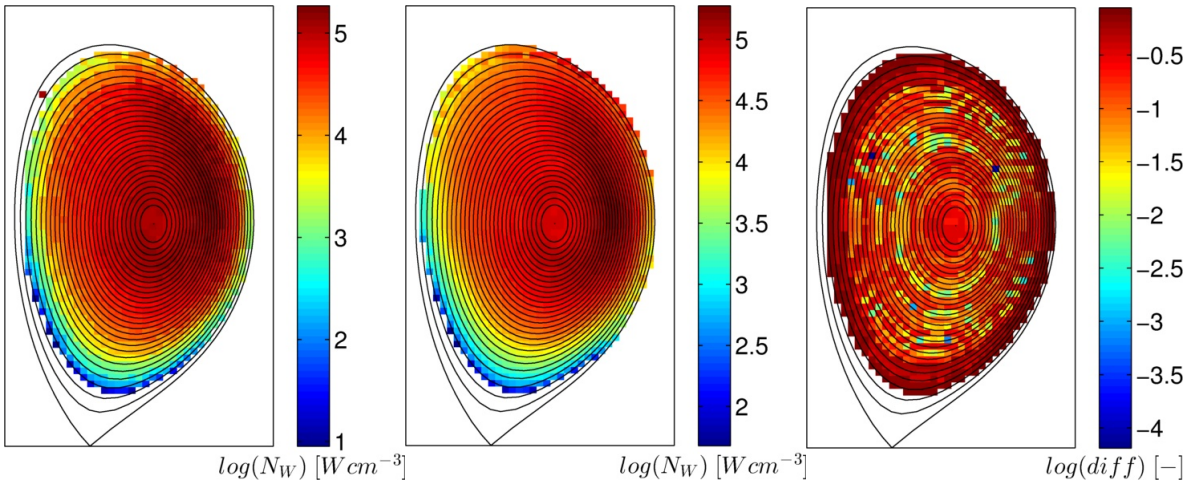

(a) $n_e(i,j)$ (b) $n_e = 8.9 \cdot 10^{13} cm^{-3}$ (c) $diff$

Figure 4.24: Estimated tungsten density in the plasma for the data set T_82722_45p2s. Results in (a) are based on calculations with the electron density profile. Results in (b) are based on calculations made with the constant n_e. The figure (c) displays the difference between results in (a) and (b) , normed to (b).

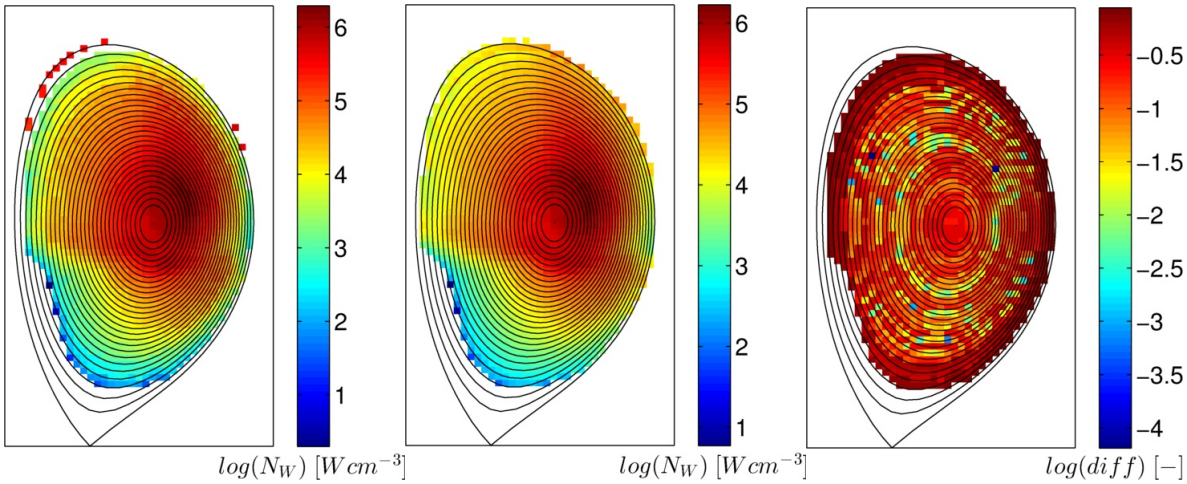

(a) $n_e(i,j)$ (b) $n_e = 8.9 \cdot 10^{13} cm^{-3}$ (c) $diff$

Figure 4.25: Estimated tungsten density in the plasma for the data set T_82722_46p3s. Results in (a) are based on calculations with the electron density profile. Results in (b) are based on calculations made with the constant n_e. The figure (c) displays the difference between results in (a) and (b) , normed to (b).

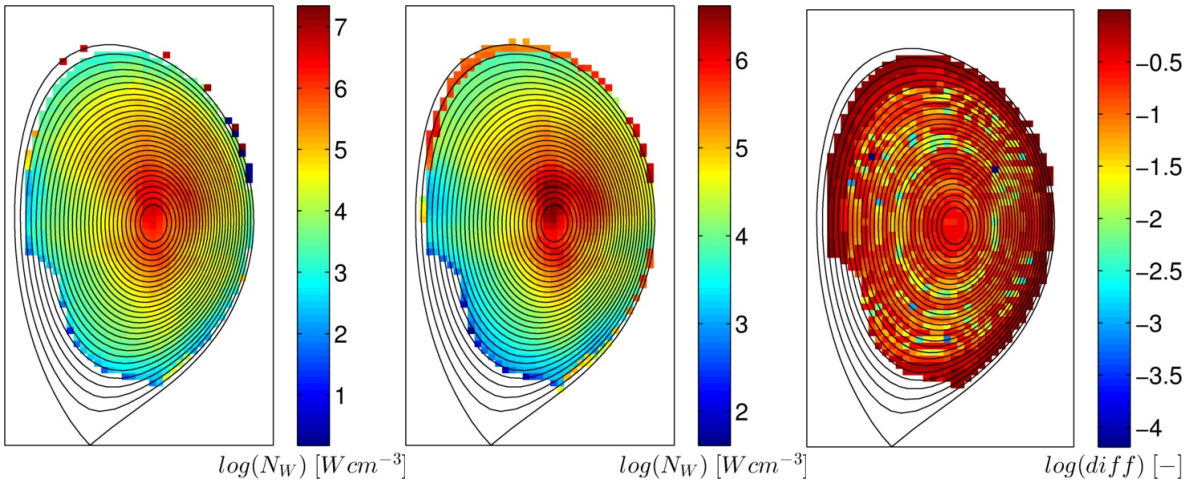

(a) $n_e(i,j)$ (b) $n_e = 8.9 \cdot 10^{13} cm^{-3}$ (c) $diff$

Figure 4.26: Estimated tungsten density in the plasma for the data set T_82722_47p5s. Results in (a) are based on calculations with electron density profile. Results in (b) are based on calculations made with the constant n_e. The figure (c) displays the difference between results in (a) and (b) , normed to (b).

4.9 Values of Correction Coefficients for Tomographic Reconstruction

Once the values of electron and tungsten densities are available, the correction coefficients for tomographic reconstructions can be computed. The estimation of the correction coefficient in the pixel i, j is has been done according to previously computed values of the electron and tungsten densities and to values of the radiation coefficients:

$$C|_{i,j} = \left. \frac{n_e^2 R_{V,ff}(T_e) + n_e N_T R_{V,l}(T_e)}{n_e^2 R_{H,ff}(T_e) + n_e N_T R_{H,l}(T_e)} \right|_{i,j} \tag{4.16}$$

where the recombination term was neglected due to its small importance. The results of correction coefficients for all three data sets are plotted in fig. 4.27, fig. 4.28, fig. 4.29. As in previous figures, results in sub-figures (a) are based on results obtained using non-constant electron density profile, in sub-figures (b) results obtained with method using constant electron density are displayed. In sub-figures (c) the difference between both groups of results normed to results based on constant electron density are displayed. The differences between both methods are again negligible.

An important conclusion from the profile of correction coefficients can be drawn after comparing it with profiles for tungsten densities and electron temperatures. The C profile follows the distribution of T_e and does not seem to be influenced by the density

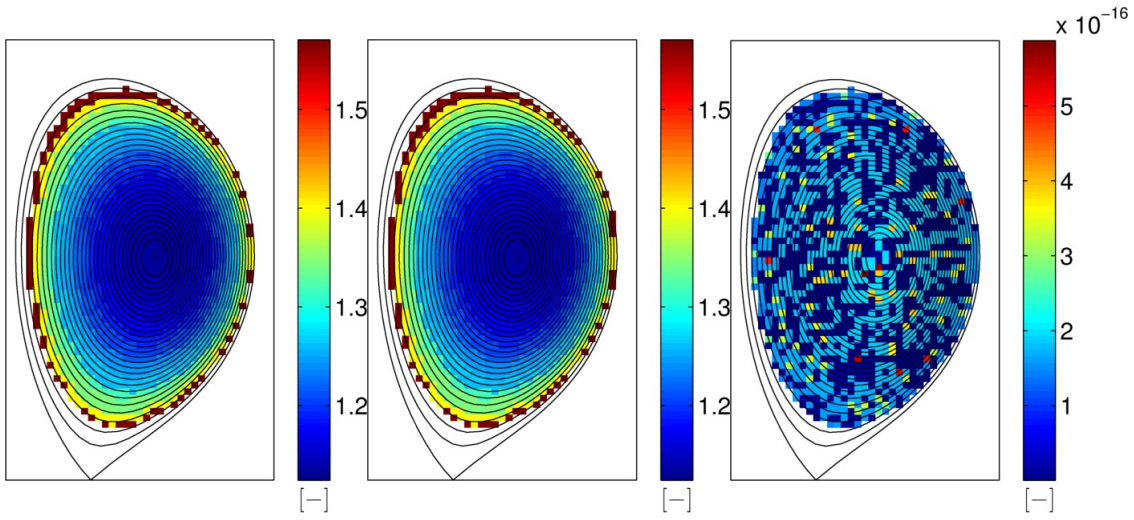

(a) $n_e(i,j)$ (b) $n_e = 8.9 \cdot 10^{13} cm^{-3}$ (c) $diff$

Figure 4.27: Correction coefficients for tomography for the data set T_82722_45p2s. Coefficients in (a) are based on the data obtained with the electron density profile. Results in (b) were calculated by using the constant electron density. The figure (c) displays the difference between results in (a) and (b) , normed to (b).

profiles. This behavior can be understood by comparing contributions of line and free-free radiation. For $S_{ff} << S_l$ the first terms in the nominator and the denominator in eq. (4.16) can be neglected and the formula can be rearranged as:

$$C|_{i,j} = \left. \frac{R_{V,l}(T_e)}{R_{H,l}(T_e)} \right|_{i,j} \tag{4.17}$$

The dependence on n_e and n_i cancels out and the value of the correction coefficient can be obtained as a ration of radiation coefficients for the vertical and the horizontal cameras. A similar situation rises for scenario in which $S_{ff} >> S_l$. In this case, the contribution of line radiation in fig. 4.16 can be neglected and the value of the correction coefficient is obtained as a ratio of radiation coefficients for the free-free radiation

$$C|_{i,j} = \left. \frac{R_{V,ff}(T_e)}{R_{H,ff}(T_e)} \right|_{i,j} \tag{4.18}$$

An order of magnitude estimate of validity of both regimes can be made by comparing the values of R_{ff} and R_l. The radiation coefficient for line radiation R_l is $\approx 10^{-24}$ and the coefficient for free-free radiation R_{ff} is $\approx 10^{-36}$. Both contributions will be equal

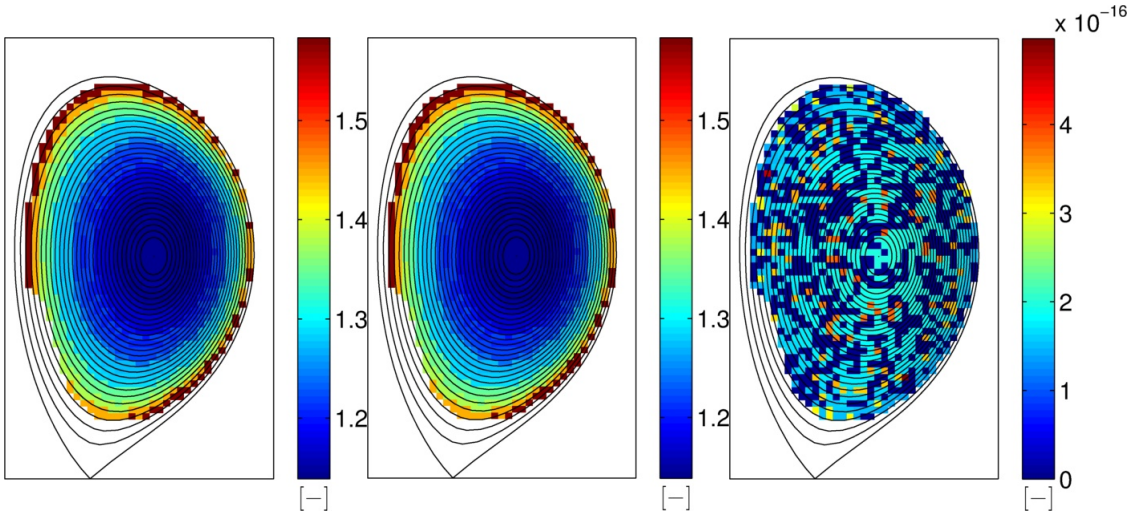

(a) $n_e(i,j)$ (b) $n_e = 8.9 \cdot 10^{13} cm^{-3}$ (c) $diff$

Figure 4.28: Correction coefficients for tomography for the data set T_82722_46p3s. Coefficients in (a) are based on the data obtained with the electron density profile. Results in (b) were calculated by using the constant electron density. The figure (c) displays the difference between results in (a) and (b) , normed to (b).

for:

$$\begin{aligned} \frac{10^{-24} n_e N_T}{10^{-37} n_e^2} &= 1 \\ \frac{n_e}{N_T} &= 10^{12} \end{aligned} \tag{4.19}$$

Based on these results it can be stated that:

- For density ratios $n_e/N_T >> 10^{12}$ the contribution of line radiation can be neglected and the correction coefficient in a pixel can be found with eq. (4.18).
- For density ratios $n_e/N_T << 10^{12}$ the contribution of free-free radiation is negligible and the correction coefficient can computed using eq. (4.17).

The density of tungsten ions is assumed to be negligible in the data set T_81835_51p1s. Values of correction coefficients for this data set were computed using formula eq. (4.18) and are displayed in fig. 4.30. The differences in results of methods of obtaining correction coefficients using eq. (4.17) and eq. (4.16) are plotted in fig. 4.31, fig. 4.32, fig. 4.33. In sub-figures (a) correction coefficients based on eq. (4.16) are plotted. Sub-figures (b) display results of correction coefficients obtained using the formula eq. (4.17) and sub-figures (c) show the differences between both methods normed to results in (a). The differences in all three datasets are negligible.

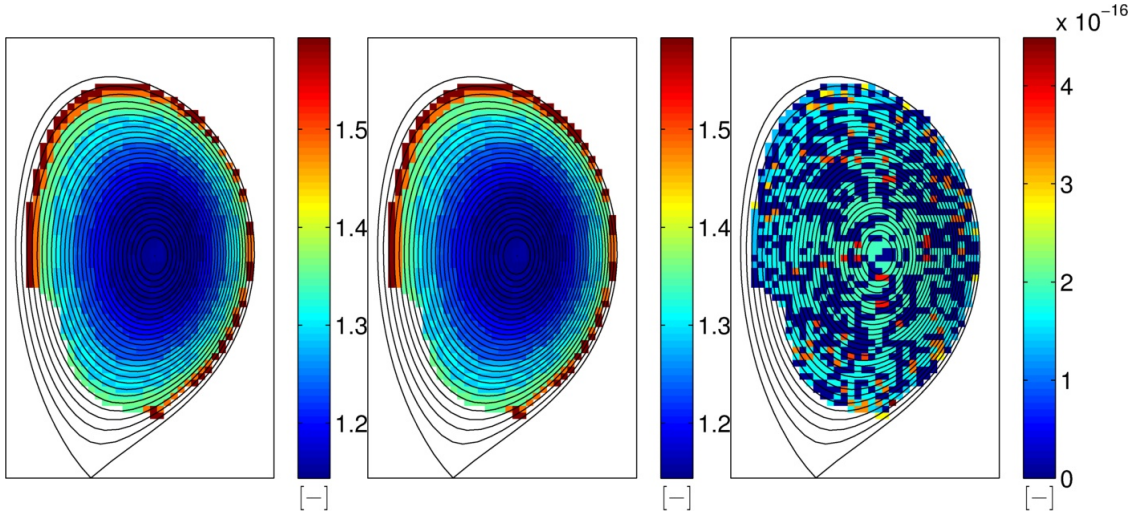

(a) $n_e(i,j)$ (b) $n_e = 8.9 \cdot 10^{13} cm^{-3}$ (c) $diff$

Figure 4.29: Correction coefficients for tomography for the data set T_82722_47p5s. Coefficients in (a) based on data obtained with non-constant electron density profile. Results in (b) were calculated by using constant the electron density. The figure (c) displays the difference between results in (a) and (b) , normed to (b).

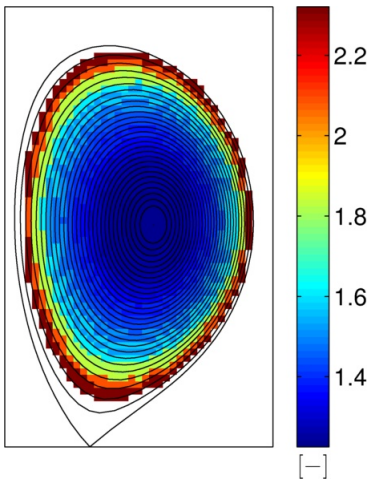

Figure 4.30: Correction coefficients for data set T_81835_51p1s. Obtained applying eq. (4.17).

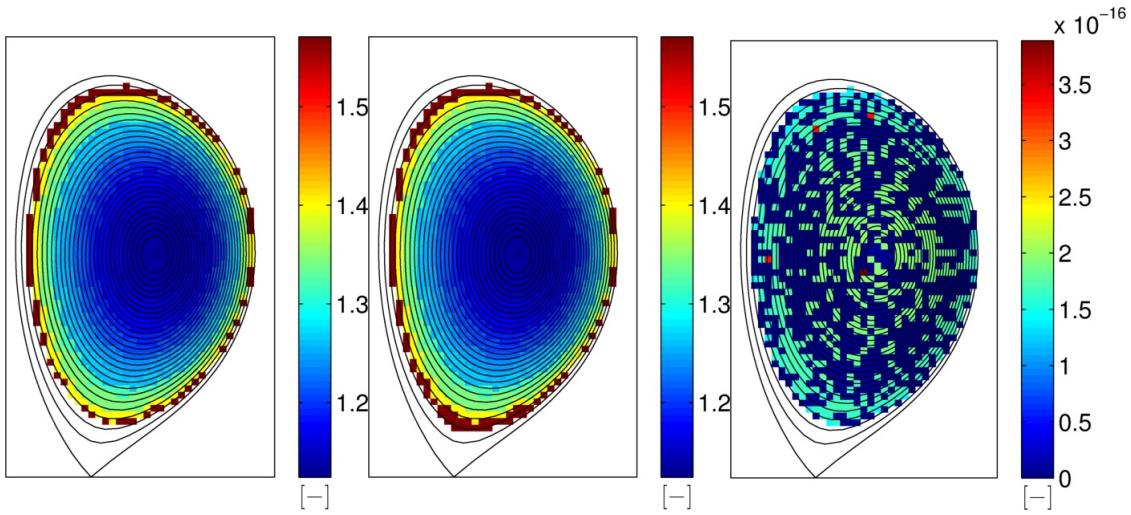

(a) (b) (c)

Figure 4.31: Comparison of the correction coefficients for the data set T_82722_45p2s obtained by using eq. (4.16) in (*a*), by using eq. (4.17) in (*b*) and the difference in both methods normed to (*a*) is displayed in (*c*).

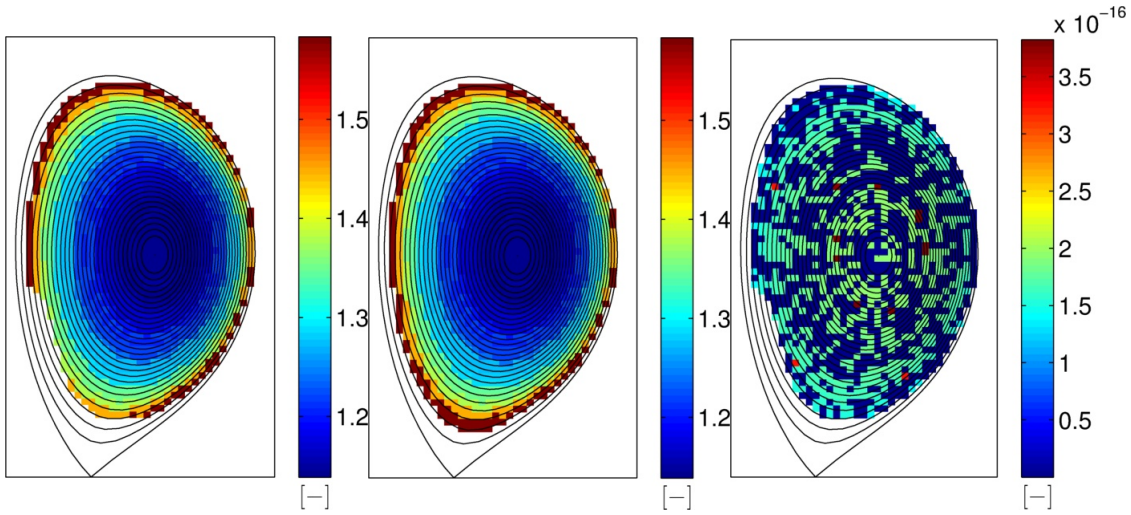

(a) (b) (c)

Figure 4.32: Comparison of correction coefficients for data set T_82722_46p3s obtained by using eq. (4.16) in (*a*), by using eq. (4.17) in (*b*) and the difference in both methods normed to (*a*) is displayed in (*c*).

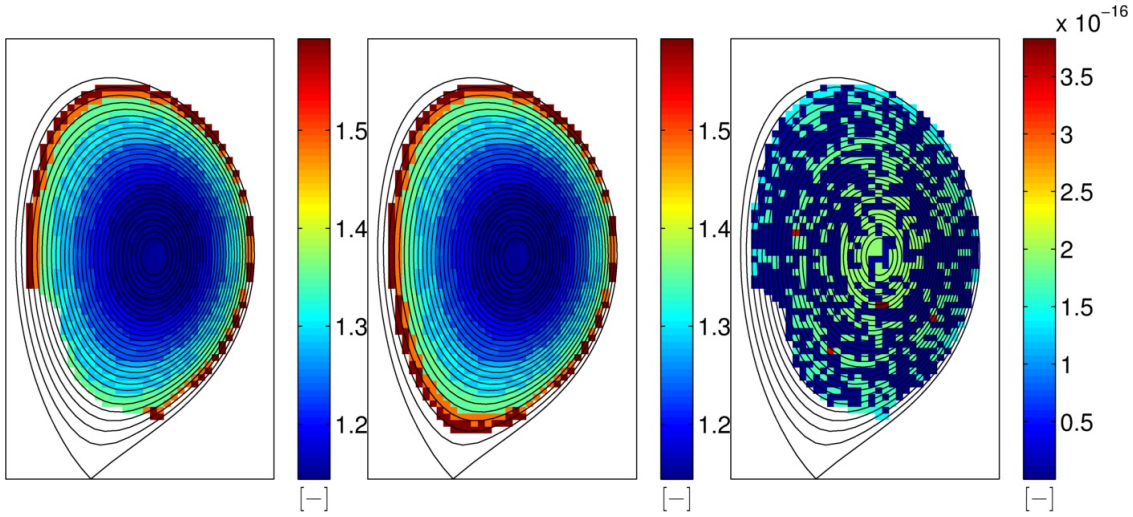

(a) (b) (c)

Figure 4.33: Comparison of correction coefficients for data set T_82722_47p5s obtained by using eq. (4.16) in (*a*), by using eq. (4.17) in (*b*) and the difference in both methods normed to (*a*) is displayed in (*c*).

Conclusions

Nuclear fusion is a promising source of energy for humanity. The main advantages are abundance of the fuel and the environmental friendliness. The fuel planned to be used in future fusion power plants is hydrogen and lithium. Both elements are common on earth and easily accessible to all countries. Fusion power plants also do not produce any carbon emissions during the energy generation and the produced waste is radioactive but its half-life is tens of years. The main disadvantage is that the fusion technology is not yet sufficiently enough to make construction of commercial power plants possible. It will still take a lot of effort and many years befor the first commercial fusion power plants can to be built.

The optimal temperature for fusion of deuterium-tritium ions is approximately 100keV. The rate of fusion reactions in a gas heated up to these temperatures is very low. The main concern about generating energy with fusion is heating up gas consisting of the deuterium-tritium mixture and maintaining the temperature. The gas at such temperatures will be in form of plasma. In order to generate power efficiently, enough fusion reactions delivering more energy than is used for the heating have to occur in the gas. it is therefore of crucial importance to reduce the energy losses from the plasma. One way of achieving this is magnetic confinement. It uses the Lorentz force to confine electrons and ions in a specific volume in order to reduce energy losses. This principle is applied in tokamaks, which are fusion devices with toroidally shaped vessels. The confinement is never perfect and some particles of the plasma can get into contact with the wall of the vessel. In this case some particles of the reactor wall can be sputtered into the plasma. These generally unwanted particles are called impurities. If an impurity particle is a light chemical element, it is ionized to the form of bare nuclei in the fusion plasma. Its influence on the quality of confinement is not significant. However, this does not valid for heavier chemical elements. The atoms are not ionized to a state of bare nuclei and they greatly increase rate of energy losses. This is caused by line radiation of impurities. Electrons in orbitals of heavy impurities are constantly excited to higher energy levels. Energy absorbed during excitation is radiated from

plasma after the spontaneous deexcitation of the ion. This radiation is called the line radiation and is one of the major mechanisms lowering the quality of the confinement.

Hot plasma tomography is a non-invasive method of studying fusion plasma profiles. From intensities measured along different poloidal directions, tomographic algorithms can reconstruct intensities for the whole plasma cross-section. This is convenient since various phenomena in plasma can be studied in this way, e.g. densities of impurities. To measure intensities along the different poloidal paths, pinhole cameras are used. They consisit of arrays of diodes sensitive to a radiation within a limited frequency range. By positioning diodes into an array, the line of sight of each diode varies from the others and the whole plasma cross-section is covered. In this work tomographic reconstructions of soft x-ray radiation generated in plasma were analyzed.

Joint European Torus is a tokamak reactor built in Culham, England. The inner wall of JET's vessel is constructed of beryllium and tungsten. Beryllium is a light chemical element which does not contribute to the line radiation, if atoms of the wall are sputtered into the plasma. Beryllium is used for the parts of the reactor wall which are not to be in contact with plasma frequently. The parts of the vessel wall which are supposed to sustain heavy heat loads and frequent contact with plasma are made of tungsten. Tungsten is a heavy metal with the highest melting point of all chemical elements. This is convenient because it lowers the possibility of damaging the inner side of the wall. The amount of atoms sputtered during a contact with plasma is small. The disadvantage of tungsten usage is the fact that tungsten is a heavy element with atomic number 74. Its atoms are not ionized into the form of bare nuclei even in the hottest parts of the fusion plasma. This causes a rapid decrease in the quality of confinement because the contribution to the energy losses by line radiation is significant, even for small densities. Tungsten densities in the JET plasma can be studied by installed tomography system. It consists of two soft x-ray pinhole cameras; one aligned in the vertical and one aligned in the horizontal direction. Due to construction constrains the thickness of the wall in front the cameras from the plasma differs. In case of the vertical and the horizontal camera, the thickness of the beryllium wall separating it from plasma is $250\mu m$ and $350\mu m$, respectively. Beryllium acts as a filter within the soft x-ray range and the different thickness of the wall causes spectral sensitivities of cameras to vary. This creates a problem for tomographic reconstructions since intensities measured by the cameras are different. The presence of tungsten impurities influenced the magnitude

of the errors observed. A way to lower the errors was suggested by Assoc. Prof. Jan Mlynař. By estimating the influence of spectral sensitivities of the cameras on the measured intensities the values of the correction coefficients were to be evaluated and used to lower the errors.

For purposes of estimation of the correction coefficients, three mechanisms of soft x-ray generation by plasma containing tungsten impurities had to be analyzed. The distribution of charge states of tungsten in the plasma had to be found as the first step. This was done by applying ionization and recombination coefficients to the ionization balance model. The values of the coefficients were provided my OPEN-ADAS [17]. The dependence of the distribution on the input parameters electron density and temperature were examined. Results show that the dependence on the electron density was very weak. It was discovered that using constant electron density $n_e = 10^{13}$ in future estimations of ionization balance will deliver sufficiently accurate results. Knowing the distribution of ionic states, the spectral properties of generated x-ray radiation were modelled. Bremsstrahlung was separated into the contribution of the free-free and of the free-bound radiation. The free-free spectrum was modelled by using the analytically derived formula and corrections by Gaunt factors were made. The free-bound spectrum produced by recombination of electrons with tungsten ions was obtained by evaluating analytically derived equations. The input of the model were ionization energies of ionic states and the distribution of ion charge states. The line radiation spectra generated by spontaneous deexcitation of tungsten ions were modelled by applying photon emission coefficients to the distribution of ionic states of tungsten. The powers were compared within the temperature range 1–4keV. The power was normed to the densities of particles involved in the mechanism of generating the particular spectra. The highest contribution was by the line radiation in orders of $10^{-23}Wcm3$. The contributions of free-free and free-bound radiation were in the order of $10^{-36}Wcm^3$ and $10^{-37}Wcm^3$, respectively. Due to the insignificance of the free-bound radiation, it was disregarded in the following analysis.

In order to study the difference in intensities measured by vertical and horizontal cameras, the spectral sensitivities of the cameras were used to filter the modelled spectra. The power carried by the filtered spectra were compared for both cameras. It was discovered that the difference in measured intensities strongly depends on the electron temperature. In order to find the values of the correction coefficients for

tomographic reconstructions, the electron temperature profile has to be known. A formula giving values for the correction coefficients was suggested. The information required are electron temperature, electron density and tungsten density.

Four sets of data were available for data analysis. They contained information about temperature profiles and tomographic reconstruction of radiation power density as measured by the horizontal camera. After examination it was assumed, that the density of tungsten in the data set labeled T_81835_51p1s is negligible. If the plasma does not contain any impurities, the only contribution to the radiation is by the free-free radiation. This set was used for an estimation of electron density profile. Two estimation methods for the contribution of the free-free and the line radiation were used. The first method was based on the obtained electron density profile. The second method used a constant value of electron density which was based on the density profile. The estimates of tungsten densities were based on the modelled contributions of the line and the free-free radiation. The highest obtained tungsten densities were in the order of $10^7 cm^{-3}$. The comparison of the tungsten densities delivered by both methods showed that the differences in the results are negligible. The more convenient way for estimation of the tungsten density is therefore the one based on the constant electron density. This is due to the lower complexity of the solved problem.

The correction coefficients were estimated for all four sets of data. The input values were:

- provided electron profiles
- tomographic reconstrucions of radiation power densities
- estimated electron densities
- estimated tungsten densities
- modelled contribution of soft x-ray radiation filtered by the spectral sensitivities of the cameras

Examining the results for correction coefficients showed that the formula can be simplified for extreme cases of tungsten densities. This is caused by the ratio of contributions of the line and the free-free radiation. If it applies for the density ratio $n_e/N_T >> 10^{12}$,

the contribution of the line radiation can be neglected. If the ration fulfills the condition $n_e/N_T << 10^{12}$ the contribution of the free-free radiation can be neglected. In both cases the dependency on the particle density cancels out and the values of the correction coefficients are governed only by the electron temperature. This greatly simplifies the algorithm for estimation of the correction coefficients.

The future work on this thesis will include application of the algorithm for evaluation of correction coefficients to the tomographic algorithms used for JET. An iterative approach with the following steps is being considered.

- The tomographic reconstruction is made based on the measured data.
- The values of correction coefficients are estimated and applied to the reconstructed data.
- The corrected data are used to repeat the tomographic reconstruction.

The number of iterations has to be suggested based on the accuracy of the data. The accuracy of the created models for the soft x-ray spectra has to be verified comparing the results to the other models. The hypothesis for extreme values of tungsten densities has to be tested and the accuracy of delivered results have to be found.

Bibliography

[1] Jeffrey P. Freidberg. *Plasma physics and fusion energy*. Cambridge University Press, 2007.

[2] G M McCracken. *Fusion the energy of the universe*. Ed. by P. E. Stott. Burlington, MA: Elsevier Academic Press, c2005, 1 online resource (xx, 186 p.) :

[3] Donald A Gurnett and A Bhattacharjee. *Introduction to plasma physics*. New York: Cambridge University Press, 2005.

[4] Francis F. Chen. *Introduction to plasma physics and controlled fusion*. 2nd ed. New York: :Plenum Press, c1984-.

[5] John Wesson and D Campbell. *Tokamaks*. 3rd ed. Oxford University Press, 2004.

[6] *European Fusion Development Agreement*. Culham, © 2001 - 2014. URL: `http://www.efda.org/jet/`.

[7] J. Mlynar et al. "Introducing minimum Fisher regularisation tomography to AXUV and soft x-ray diagnostic systems of the COMPASS tokamaka)". In: *Review of Scientific Instruments* 83.10, 10 (2012).

[8] M. Odstrcil et al. "Modern numerical methods for plasma tomography optimisation". In: *Nuclear Instruments and Methods in Physics Research Section A: Accelerators, Spectrometers, Detectors and Associated Equipment* 686.0 (2012), pp. 156 –161. ISSN: 0168-9002. DOI: `http://dx.doi.org/10.1016/j.nima.2012.05.063`. URL: `http://www.sciencedirect.com/science/article/pii/S0168900212005712`.

[9] J. Mlynář et al. "2D tomography of SXR data from toroidally separated cameras for studies of impurity injection and fast instabilities on JET". In: *30th EPS confernce on Plasma Physics* (2011).

[10] Randy Harris and Randy Harris. *Modern physics*. 2nd ed. Pearson/Addison Wesley, c2008.

[11] G V Pavlinksy. *Fundamentals of x-ray physics*. Cambridge: Cambridge International Science Pub., 2008, 1 online resource (xiv, 245 p.) :

[12] I H Hutchinson. *Principles of plasma diagnostics*. 2nd ed. Cambridge: Cambridge University Press, 2002, xvii, 440 s. :

[13] David Salzmann. *Atomic physics in hot plasmas*. New York: Oxford University Press, 1998, 1 online resource (viii, 263 p.) :

[14] T J M Boyd. *The physics of plasmas*. Ed. by J. J. Sanderson. Cambridge, UK ; Cambridge University Press, 2003, 1 online resource (xii, 532 p.) :

[15] Eberhard Haug. *The elementary process of Bremsstrahlung*. Ed. by Werner. Nakel. River Edge, NJ: World Scientific, c2004, 1 online resource (x, 259 p.) :

[16] Whiteford. *On the spectral emission of impurity species for diagnostic application to magnetically confined fusion plasmas*. doctoral thesis. University of Strathclyde, 2004. URL: http://www.adas.ac.uk/theses/whiteford_thesis.pdf.

[17] *OPEN-ADAS*. 1995-2014. URL: http://open.adas.ac.uk/.

[18] Alexander E. Kramida and Joseph Reader. "Ionization energies of tungsten ions: W2+ through W71+". In: *Atomic Data and Nuclear Data Tables* 92.4 (2006), pp. 457 –479. ISSN: 0092-640X. DOI: http://dx.doi.org/10.1016/j.adt.2006.03.002. URL: http://www.sciencedirect.com/science/article/pii/S0092640X06000167.